Supplementary information for

Organization of Historical Oceanic Overturnings on Cross-Sphere Climate Signals

by

Yingjing Jiang[1], Shaoqing Zhang[1*], Yang Gao[2*], Lixin Wu[1,3*], Lv Lu[1], Zikuan Lin[1], Wenju Cai[1, 3], Deliang Chen[4, 5], L. Ruby Leung[6], Bin Wang[7], Xueshun Shen[8], Mingkui Li[1], Xiaolin Yu[1], and Xiaopei Lin[1]

[1]Key Laboratory of Physical Oceanography, Ministry of Education/Frontiers Science Center for Deep Ocean Multispheres and Earth System/College of Oceanic and Atmospheric Sciences, Ocean University of China, Qingdao, China

[2]Frontiers Science Center for Deep Ocean Multispheres and Earth System/Key Laboratory of Marine Environmental Science and Ecology, Ministry of Education, Ocean University of China, Qingdao, China

[3]Laoshan Laboratory, Qingdao, China

[4]Department of Earth System Sciences, Tsinghua University, Beijing, China

[5]Department of Earth Sciences, University of Gothenburg, Gothenburg, Sweden

[6]Atmospheric, Climate, & Earth Sciences Division, Pacific Northwest National Laboratory, Richland, WA, USA

[7]Department of Atmospheric Sciences and International Pacific Research Center, University of Hawaii at Manoa, Honolulu, HI, USA

[8]The Center of Earth System Modeling and Prediction, CMA, Beijing, China

Contents of this file

Text S1-S3:

Text S1: Convergent atmospheric and oceanic states in CDA estimates

a, Convergent atmospheric mean meridional circulation (AMMC) mean states

The AMMC is denoted as the temporal mean atmospheric meridional stream function, which can be expressed following Sun & Zhou [68] and Jiang et al. [30] as:

$$\Psi = \frac{2\pi a cos\emptyset}{g}\int_0^p \bar{v}dp\,. \qquad (Eq.S1)$$

Here, $\bar{v}$ is the zonal average meridional wind, p is the pressure, $\emptyset$ is the latitude, g is the gravitational acceleration, and a is the radius of the Earth.

In a manner similar to the definition of the GMOC index (see **Methods**), we define the AMMC index as the linear regression coefficient of the monthly AMMC with respect to its temporal mean value obtained from ERA5.

Figure S4 shows the root-mean-square error (RMSE) distributions of AMMC for model simulations and CDA estimates against ERA5. The large errors of model-simulated AMMC are distributed over the tropics and areas lying at 60°–80° S in the Southern Hemisphere (SH). The tropical error of CM2-HIS is larger than that of CESM-HIS, which can be attributed to the coarser resolution of the atmospheric model in CM2. The substantial errors in these regions could potentially affect the accuracy of subsequent analyses related to the AMMC and its interaction with other climate components. The observational constraint greatly reduces the error of the AMMC in both CDA experiments. The improvement in CM2-CDA is larger than that in CESM-CDA. This indicates that observational data play a crucial role in enhancing the accuracy of AMMC estimates, and the greater improvement in CM2-CDA suggests that it may benefit more from the incorporation of observational information as compared with CESM-CDA. The AMMC obtained via CDA is generally consistent with ERA5 (**Fig.S4e&f**), although it is a little weaker at high latitudes.

b, Convergent ocean temperature and salinity estimates

By analyzing the time series of ocean temperature and salinity at different depths (0–500, 500–2000, and 2000–5000 m) over the latitude range of 60° S–60° N (as shown in **Fig.S1**), we note that, although systematic differences between CDA estimates (CESM-CDA and CM2-CDA) and the objective analysis product EN4 exist, they are much smaller when compared with the differences between model simulations (CESM-HIS and CM2-HIS) and the EN4 product. Moreover, the phases in the variations of CDA-estimated ocean temperature and salinity are highly consistent with EN4.

We also present the results of other CDA experiments, namely CESM-CDA0 and CM2-CDA0, which were initialized with different initial conditions on January 01, 1978. These experiments have been evaluated in Jiang et al. [30].

Both CDA systems converge from different initial conditions that are produced from different coupled spin-up states (CESM-CDA0 starts from the historical simulation on 01-01-1869 and CM2-CDA0 starts from the previous assimilation on 01-01-1978 from Chang et al. [69]. This convergence indicates that the CDA method possesses a certain robustness in handling different initial setups, which is crucial for obtaining reliable and consistent results in the context of oceanographic studies.

Although coherent convergence of upper- and deep-ocean temperature and salinity in CDAs to the EN4 observation product occurs, the CDA results are somewhat sensitive to the change in oceanic observing system as the Argo profiles are assimilated (see the period after 2000 in **Fig.S1c–d**). This sensitivity implies that further investigations are needed to understand how the CDA performance might be affected by different configurations of the oceanic observing system, and to develop strategies to mitigate potential uncertainties introduced by such changes.

***c*, Convergent estimation of atmospheric work exerted on the ocean and oceanic heat fluxes to the atmosphere**

To gain an understanding of the balance between the atmosphere and ocean achieved through CDA, we conduct an examination of air–sea interaction processes within the CDA framework. To quantitatively assess the atmospheric work exerted on the ocean (W_{A2O}), we utilize the following formula based on Huang et al. [70]:

$$W_{A2O} = \tau_x * u^O + \tau_y * v^O, \qquad (Eq.S2)$$

where, (τ_x, τ_y) are the wind-stress at the sea surface and (u^o, v^o) are the sea surface currents (for verification with "observation", we use geostrophic currents in this case).

Figure S2 presents the error distributions of W_{A2O} for both model simulations and CDA results in comparison with the observed product, as well as the time series of the global mean W_{A2O}. The observed sea surface wind-stress is obtained from ERA5, while the geostrophic currents are derived from the Archiving, Validation and Interpretation of Satellite Oceanographic data (AVISO). **Figure S2a&b** shows that the errors of model simulations are substantial in low-latitude areas of the North Pacific, areas near 20° S in the Indian Ocean, and ACC areas of the Southern Ocean. The substantial errors in these regions may potentially lead to inaccuracies in subsequent analyses related to air–sea interaction processes and climate model predictions. In addition, the errors are also substantial in the areas of the Kuroshio, Gulf Stream, and near 10° S in the Pacific.

The much smaller errors of W_{A2O} obtained via CDA compared with the corresponding model simulation not only indicate its superiority in approximating the actual situation but also suggest that it can provide more reliable estimates for further studies on air–sea interaction dynamics. From the time series of the normalized W_{A2O}, we observe that the error of the CESM is approximately 1 mW/m^2 larger than that of the CM2. We also note that, in addition to reducing the W_{A2O} bias, CDA substantially corrects the phases of W_{A2O} variability. This correction is of great importance because it can enhance the accuracy of predicting air–sea interaction phenomena based on W_{A2O}.

To analyze the oceanic heat flux to the atmosphere, we examine it through the surface turbulent heat flux (HF_{O2A}), which consists of sensible (Q_S) and latent (Q_L) heat fluxes as described by Cronin et al. [71]. The relationship can be expressed as:

$$HF_{O2A} = Q_S + Q_L. \qquad (Eq.S3)$$

Figure S3 plays a crucial role in illustrating the error distributions and RMSE time series of HF_{O2A} for both model simulations and CDA results in comparison with ERA5. It provides valuable insights into the performance of different models and CDA methods. We observe that large positive and negative values of HF_{O2A} errors are distributed over high latitudes of the North Atlantic and Southern Ocean ACC areas in model simulations (**Fig.S3a&b**). The presence of such large positive and negative values of HF_{O2A} errors in these regions may potentially lead to inaccuracies in predicting the response of the climate system to ocean–atmosphere heat exchange and could affect subsequent analyses related to air–sea interaction dynamics.

There are also substantial errors in tropical oceans and areas of the Kuroshio and its extension, where strong air–sea interactions occur [42]. The substantial reduction of heat flux errors by CDA compared with model simulation, especially in high latitudes of the North Atlantic and ACC areas, indicates that CDA can effectively correct inaccuracies in estimating the oceanic heat flux to the atmosphere. This improvement is of great importance because it enhances the reliability of climate models in simulating the heat exchange process between the oceans and atmosphere.

From the RMSE time series of HF_{O2A} (**Fig.S3e**), we observe that although the errors of CDAs are substantial reduced compared with those of their corresponding model simulations, they still exhibit consistent variation phases. This consistency implies that CDAs maintain a certain level of stability in estimating the oceanic heat flux to the atmosphere, despite the reduction in error magnitudes.

Text S2: More evaluations of CDA-estimated GMOC mean state and variability

a, Convergent upper-ocean circulations in CDA-estimated GMOC

From **Fig.1a–d**, we note that although both CDA estimates generally result in consistent changes in circulation patterns, there are nuanced differences in the GMOC behaviors during the transitions from CESM-HIS to CESM-CDA and from CM2-HIS to CM2-CDA. Specifically, the transport center between 10° and 30° S within the 500–2000 m depth range is more intense in CESM-CDA than in CM2-CDA, by at least 5 Sv. Additionally, the transport associated with the North Atlantic Deep Water (NADW) is somewhat stronger in CM2-CDA than in CESM-CDA in terms of both its central strength and vertical penetration. Moreover, the southward return circulation in the deep ocean is considerably stronger in CM2-CDA than in CESM-CDA, especially for the branch at the equator.

To validate ocean current velocities at a depth range of 950–1150 m, we utilize the "observation" data derived from Argo-drift information [34], as shown in **Extend Data Fig.1**. As pointed out by Su et al. [34], there are widespread global discrepancies between modeled and observed mid-depth ocean currents. Here, we observe that, in general, the models underpredict current velocities globally, and this global underestimation may lead to inaccuracies in understanding the overall ocean circulation patterns and related physical processes. The underprediction is especially pronounced over the tropics and mid-latitudes.

The ocean current velocity distributions of SODA3 and ORAS5 are similar to that of CDA estimates, while ECCO4 is close to the model simulations, which underestimate the current velocity. From the perspective of average velocity, ECCO4 is too small, while CESM-CDA and CM2-CDA are closest to Argo-drifting compare to ocean reanalysis products. From the distribution of RMSE, CEMS-CDA and CM2-CDA are significantly smaller than SODA3 and ORAS5, especially in the ACC region of the southern hemisphere and between 35° N and 75° N in the northern hemisphere. This finding suggests that the circulation center of the CDA-estimated GMOC, located between 10° and 30° S at a depth range of 500–2000 m, is highly likely to be realistic.

b, Convergent deep-ocean circulations in CDA-estimated GMOCs

In deep portions of the oceans, current velocities simulated by the models herein are generally small (as shown in **Fig.S5a&b**). Large-value regions are predominantly concentrated along the western boundary of the Atlantic and in the Antarctic Circumpolar Current (ACC) areas, with a maximum velocity reaching 2 cm/s. In contrast, in other regions, the velocities of ocean currents are generally less than 0.5 cm/s.

We note that in open deep-ocean regions, such as the Pacific and central South Atlantic, the current velocities of the CESM are larger than those of the CM2, and the CESM provides greater detail. This may be attributed

to the fact that the CESM has a slightly higher horizontal and vertical resolution compared with the CM2.

The deep-ocean currents estimated by CDA are substantially enhanced globally compared with the model simulations (**Fig.S5c&d**), although the increases in the ACC and WBC areas are relatively small. This accounts for the enhancement of the deep-circulation system of GMOC in CDA estimates.

Owing to the lack of observations in deep portions of the oceans below 2000 m, we are unable to determine whether this enhancement aligns with the real-world situation. However, considering the improvement in the 1000-m current velocities, balanced atmosphere–ocean coupling system, and constraints on deep-ocean model biases, we infer that the deep-ocean current velocities of CDA approach real-world values.

***c*, Decomposition of AMOC and IPMOC (Indo-Pacific meridional overturning circulation) of GMOC**

The AMOC, being an important component of GMOC, plays a crucial role in both local and global climates [72]. In **Fig.S6a–d**, the mean states of the AMOC for model simulations and CDA estimates are presented. Meanwhile, in **Fig.S6e–g**, the corresponding versions of ocean reanalysis products are presented. The mean states of the AMOC in CESM-HIS and CM2-HIS exhibit a similar characteristic, featuring northward flows in the upper 1000 m and southward flows in the 1500–3000 m depth range. The intensity of the upper circulation of the AMOC in CESM-HIS is marginally stronger than that in CM2-HIS. In contrast, the strength of the deep southward transport circulation in CM2-HIS is greater than that in CESM-HIS. The CDA process substantially enhances the AMOC, and it also generates a new circulation core at a depth of 1000 m and latitude of 20° S. Consequently, in both the CESM-CDA and CM2-CDA, the AMOC displays a “double-core” northward transport circulation structure, which can be attributed to an enhanced South Atlantic subtropical gyre.

From **Fig.S6e–g**, we observe that the features of the AMOC in ocean reanalysis products appear to be intermediate between those of the model simulations (**Fig.S6a&b**) and those of the CDAs (**Fig.S6c&d**). Compared with the model simulations, the AMOCs in ocean reanalysis products exhibit strengthened circulations in the upper 3000 m of the South Atlantic and relatively small southward transport circulations in deep tropical oceans. However, unlike in the CDAs, the strengthened South Atlantic circulations do not form an enclosed circulation core. Meanwhile, the circulation cores associated with the NADW in ocean reanalysis products appear to be similar with those of the model simulations, with the latter cores remaining above 3000 m. In contrast, the corresponding CDA counterparts extend below 4000 m.

Besides presenting the IPMOCs for model simulations and CDA estimates, we also display the IPMOCs of ocean reanalysis products in **Fig.S6l–n**. Similar to the IPMOCs of the CDA estimates (as shown in **Fig.S6j&k**), the IPMOCs in ocean reanalysis products exhibit negative (southward transport) circulations, particularly in

ECCO4 and ORAS5, which are predominant over the area south of 40° N. This supports the hypothesis that the enhanced deep southward transport circulations in CDA-estimated GMOCs (shown in **Fig.1c&d**) primarily come from the data-constrained Indo-Pacific Oceans, and therefore, they are most likely realistic.

***d*, Coherent CDA-estimated ocean stratification with the observation**

Previous studies have suggested that balanced and coherent states of the atmosphere and oceans are crucial for reconstructing the three-dimensional flows and overturning circulations of the oceans through data assimilation [10,30]. Following the evaluation of the AMMC, W_{A2O}, and HF_{O2A} in **Text S1**, we investigate the ocean temperature, salinity, and potential density estimated by CDA herein to clarify the coherence of ocean stratification within our balanced CDA estimates.

We compute the RMSE reduction rates of potential density within the CDA framework relative to the ocean reanalysis results (SODA3, ECCO4, and ORAS5), with the latter being verified against the WOA (as depicted in **Fig.S7**). In comparison with the results of ocean reanalysis, the RMSE of potential density in most areas of the two CDAs significantly declines, particularly below 2000 m, with a reduction rate ranging from 60% to 80%. This finding indicates that in areas where observational data are scarce in the deep oceans, employing stronger restoration schemes can mitigate deep-ocean model biases and lead to balanced and coherent ocean stratification. In the upper middle ocean (0–2000 m), the CDA-estimated potential density, employing multiscale filtering assimilation, is also improved in many areas, especially when compared with ECCO4 and ORAS5.

***e*, Observation-convergent geostrophic GMOC mean states in CDA**

The geostrophic GMOC displays a general characteristic of positive (northward-transport) circulations in the SH and negative (southward-transport) circulations in the NH, as shown in **Fig.S8**. However, in the SH, although the geostrophic GMOCs in CDA estimates, ocean reanalysis products, and the "observation" are characterized by a large positive circulation with a small negative center in the upper 500 m of the subtropics, the positive circulation in model simulations is much smaller and weaker, and vice versa for the negative circulation. In the NH, although the CDA-estimated geostrophic GMOCs exhibit negative, positive, and negative patterns in the upper 1000 m at low, middle, and high latitudes, respectively, similar to those of ocean reanalysis products and the "observation", the patterns in model simulations are particularly weak, especially in the tropics within CESM-HIS.

The above analyses are substantiated by the distributions of differences between the two model GMOCs,

those between the two CDA-estimated GMOCs, and those among the ocean reanalysis products, as depicted in **Fig.S8**. The strong geostrophic transport in the SH may be attributed to the more open nature of the oceans in the SH, while the weaker geostrophic transport in the NH may be attributed to the more complex ocean basin structure in the NH. Owing to common discretization features, such as an approximately 100 km horizontal resolution, free model simulations tend to produce generally similar GMOC patterns. However, these patterns deviate substantially from the real world owing to the approximation of physics and omission of certain scales in the models. Our CDA results with independent models suggest that multiscale data–model incorporation, consisting of deep-ocean bias treatment, can recover the GMOC mean state by a credible degree.

***f*, Standard deviation (STD) of GMOC**

In **Fig.S9**, we show the STD values of the GMOCs for model simulations and various assimilation products. In general, large STD values of the GMOC are predominantly located in the ACC (Antarctic Circumpolar Current residual circulation), tropical, and NADW areas. However, these values are relatively lower in model simulations but much higher in ocean reanalysis products, particularly in the ACC-RC region and tropics of SODA3 and ECCO4.

Although the distribution patterns of GMOC STD values for the two CDAs and ORAS5 exhibit a generally similar characteristic, featuring high values in the tropics, deep penetration in the ACC-RC area, and relatively high values at high-latitudes of the NH, the patterns of SODA3 and ECCO4 deviate from this characteristic. Among the seven GMOC STD distributions, which include two model simulations, two CDA estimates, and three ocean reanalysis products, the two CDA estimates exhibit the same distribution centers. However, the values in CM2-CDA are larger than those in CESM-CDA (as can be seen by comparing in **Fig.S9c&d**).

We also compare the STD values of AMOCs, as shown in **Fig.S10**. The STD values of model simulations are smaller than those of assimilation results. Both CEMS-HIS and CM2-HIS exhibit a similar structure, in which, the maximum values are located in the North Atlantic at approximately 40° N and a depth of 1000–2000 m. In contrast, the maximum STD values of CESM-CDA and CM2-CDA are located in tropical oceans at a depth of 500–1500 m, comparable with those of the ocean reanalysis products SODA3 and ORAS5.

***g*, Convergent GMOC variability in CDA estimates**

To assess GMOC variability, we calculate the linear regression coefficient between GMOC states at each time slice and their mean state as a GMOC index, measuring the departure of an instant from the mean (see **Methods**). The timeseries of GMOC indices for CESM-HIS, CM2-HIS, CESM-CDA, CM2-CDA and the

mean of three reference ocean reanalysis products are displayed in **Extend data Fig.2a**. Model-simulated GMOC timeseries show little correlation (0.04), whereas the CDA-estimated GMOC timeseries are highly correlated (0.59, far above the 99% significance for 960 degrees of freedom, see **Methods**). We first check the volume transports at 47°, 26°, and 16° N in the Atlantic (where long-term observations exist), as shown in **Extend data Fig.2b–d**. The CDA- and reanalysis-estimated transports align well with observations in all three cross-sections, substantially outperforming model simulations and exhibiting correlation above the 99% significance level. All data-constrained estimates fit best at the 26° N RAPID cross-section (compare **Extend data Fig.2c** with **Extend data Fig.2b&d**), likely owing to the dominance of large-scale circulations in the mid-latitude Atlantic, which facilitates data constraints. For cross-sections at different latitudes, CDA and ocean reanalyses perform differently. In mid-to-high latitudes, both CDA estimates and ocean reanalyses show comparable quality. However, at low latitudes, CDA substantially outperforms ocean reanalysis products. This suggests that in the tropics, where air-sea interactions are highly active, the coupled data assimilation improves the efficiency of model–data integration, enhancing analysis quality.

Given the lack of direct and systematic observations on ocean currents, we evaluate the CDA-estimated GMOC by verifying its geostrophic component (see **Methods**). We further assess the variability of the CDA-estimated GMOCs by verifying their geostrophic components against "observed" geostrophic timeseries derived from an observational dataset (e.g., EN4) [35] using monthly ocean temperature and salinity data. Given that model simulations, CDA estimates, and ocean reanalysis products may have varying compositions of geostrophic and non-geostrophic components, we examine the behavior of geostrophic GMOCs across different timescales (**Extend data Fig.2e–g**). In free model simulations, aside from some correlation in the temporal mean geostrophic distribution with "observations," as expected, no correlation in variability is observed at any scale. Overall, the CDA constraint greatly improves the capability of model's geostrophic fitting, particularly in the low-frequency band. However, as timescales shorten, geostrophic fitting becomes more challenging (**Extend data Fig.2g**). At the decadal scale, CDA estimation shows slightly better skill than ocean reanalysis (0.66 vs. 0.64 for 6–10-yr mean correlation). In contrast, ocean reanalysis performs better at the interannual scale (0.51 vs. 0.41 for 1–5-year mean correlation). These differences likely arise from the distinct approaches in information capture: ocean reanalysis relies on specified "observed" atmospheric fluxes, while CDA estimation operates within a coupled model framework, which has more uncertainties in atmospheric fluxes but achieves a greater atmosphere-ocean coupling balance.

Text S3: Physical analysis of observation-convergent GMOC variability

a, Mechanisms of multiscale processes in maintaining GMOC

The GMOC is the consequence of maintaining an atmosphere–oceans balance. As important components of the Earth system, the oceans and atmosphere interact with each other in multiscale processes (**Extend Data Fig.3**). Excluding various dissipation mechanisms, the coupled atmosphere and oceans on Earth can be regarded as a semi-enclosed system [73]. In this system, the atmosphere "stirs" the oceans, while the oceans feed back to the atmosphere with updated boundary conditions that have redistributed thermal properties [74]. If the coupled atmosphere–oceans system is reduced to a two-dimensional space in the vertical and meridional directions, the atmosphere and oceans can still be viewed as a pair of zonally-averaged self-constrained counterparts, such as the AMMC [75] and GMOC [1]. The AMMC consists of Hadley, Ferrel, and Polar cells, corresponding to Earth's surface wind systems, including the trade winds and westerlies, among others (**Extend Data Fig.3a).** Under the joint influences of atmospheric wind stress, Coriolis force, and topography, the oceans ultimately form a complex circulation system (**Extend Data Fig.3b)**. Ocean water upwells in the Southern Ocean under wind-driven Ekman effects, and flows northwards to high-latitudes in the Northern Hemisphere (NH), then sinks owing to evaporation and cooling, forming the NADW that continuously transports southwards as the return flow. There are abundant and complex mixing and dissipation processes in the tropics. The variation mechanism of GMOC can be summarized as a three-term balance model [2] **(Extend Data Fig.3c)**, i.e., the residual between the difference in northern sinking and southern upwelling, subtracting tropical diffusive mixings, drives the change in pycnocline depth anomaly.

However, owing to imperfect Earth modeling and observational systems [35,76], a complete picture of the historical AMMC–GMOC mean state and variability has yet to be established. Owing to suboptimal discretization and physical schemes in climate models [77], the three-dimensional motion of ocean water simulated by models is different from that in the real world [78]. Models tend to simulate a pair of AMMC–GMOC structures with different features in their own model spaces [30]. The model GMOC is unable to represent the transport of heat, freshwater, carbon, and nutrients between the hemispheres in the real world. Moreover, measurements of ocean states are very limited [79], usually focusing on the ocean surface [80], or otherwise only available as in-situ temperature and salinity profiles for the subsurface [81]. In this study, we attempt to discover the degree to which a CDA approach can establish the AMMC–GMOC mean state and variability in a coherent and balanced manner of model–data incorporation.

We show the mean states of NADW (**Fig.1g–l**), ACC-RC (**Fig. S11**) and tropical diffusive mixing (**Fig. S12**).

For NADW, both CDA estimates produce a nearly identical isopycnal structure with the observation while ORAS5 only displays somewhat improvement from free model simulations. For ACC-RC, CDA constraints weaken the northward transport between 65°–45° S and strengthen the southward transport around 45° S at 1000–2000 m depth from free model simulations, bringing the CDA ACC-RC mean state closer to the "observation" (**Fig.S11**). Since ocean reanalysis uses "observational" atmospheric fluxes, it is expected that ORAS5 shows the best fit for the mean ACC-RC features. For tropical diffusive mixing (ε_m), while the model simulations appear very weak, especially in CESM, both CDA estimates greatly enhance ε_m in the regions of tropical instability waves, WBCs, and the southern and northern equatorial currents across the Pacific, Atlantic, and Indian basins, bringing the estimates close to the level of high-resolution (25 km) ORAS5 ocean reanalysis (**Fig.S12)**.

***b*, Decomposition of multiscale GMOC modes**

In **Fig.S14a&e**, we present the 1–20-yr band-pass filtered time series of the AMMC and GMOC. Similar to the case of GMOCs in CESM-HIS and CM2-HIS, the time series of AMMCs in CESM-HIS and CM2-HIS are almost uncorrelated, with a correlation coefficient of −0.01. While the variabilities of CESM-CDA and CM2-CDA are highly correlated, with a correlation coefficient of 0.51. On interannual to multidecadal scales, the variability of the CDA-estimated AMMC approximates to the "observed" product derived from ERA5 reanalysis. Meanwhile, the variability of the GMOC approximates the mean of the three ocean reanalysis products.

In **Fig.S14b–d**, we present the 1–20-yr band-pass filtered time series of the North Atlantic Oscillation (NAO) index, Southern Oscillation Index (SOI), and Southern Annular Mode (SAM) index. Additionally, in **Fig.S14f&h**, we present the 1–20-yr band-pass filtered time series of NADW, ε_m and ACC-RC.

The NAO employs a PC-based index, which is the time series of the leading EOF of sea level pressure (SLP) anomalies over the Atlantic sector within the range of 20°–80° N and 90° W–40° E, as defined by Hurrell & Deser [82]. The SOI is a time series that represents the monthly SLP difference between Tahiti and Darwin in the tropical Pacific, as described by Trenberth & Hoar [83]. The SAM also employs a PC-based index, which is the time series of the leading EOF of SLP anomalies over the SH within the range of 40°–65° S, as specified by Marshall [84].

Similar to the cases of the AMMC and GMOC mentioned previously, the variabilities of the NAO, SOI, SAM, NADW, ε_m, and ACC-RC in CESM-HIS and CM2-HIS are discrepant. In contrast, those in CESM-CDA and CM2-CDA converge. The NAO, SOI, and SAM estimated by CDA are in line with the ERA5

"observational" result. Furthermore, the NADWs of the two CDAs converge to the objective analysis product EN4 on decadal and multidecadal scales. However, the variabilities of the model simulations and ORAS5 are discrepant and deviate substantially from those of EN4. Moreover, the ACC-RCs of the CDAs are highly in line with both EN4 and ORAS5 on the interannual scale, corresponding to the interannual variability of wind stress. It is worth mentioning that the ε_m time series of CESM-CDA and CM2-CDA are essentially consistent after 1978, especially with regard to changes on interdecadal and annual scales.

***c*, Composite GMOC variability by NADW, ACC-RC and ε_m**

We perform EOF analysis on the GMOC stream functions in the regions north of 30° N, between 30° S and 30° N, and south of 30° S, which are referred to as $GMOC^n$, $GMOC^t$, and $GMOC^s$, respectively. Then, in **Fig.3a–i**, we present the time series of the first PC (PC1) obtained from the EOF decomposition of $GMOC^n$, $GMOC^t$, and $GMOC^s$, along with the band-pass filtered NADW, ε_m, and ACC-RC indices for CESM-HIS, CESM-CDA, and ORAS5. The counterparts in CM2-HIS and CM2-CDA are presented in **Extend Data Fig.6**.

With the exception of the CESM-HIS case, in all instances of free model simulations and data-constrained products, the PC1s of $GMOC^n$, $GMOC^t$, and $GMOC^s$ are substantially correlated with the NADW, ε_m, and ACC-RC indices, respectively. The low correlation between the $GMOC^n$ of CESM-HIS and NADW may be ascribed to the specific model deficiency in the North Atlantic [41]. This deficiency is largely rectified by the CDA data constraints, as can be seen by comparing **Extend Data Fig.6a&b**. In all data-constrained products, the correlation between the $GMOC^s$ and ACC-RC is highest, while that between the $GMOC^t$ and ε_m is lowest; the correlation between the $GMOC^n$ and NADW lies between these two. The mean correlations for the three cases in the data-constrained results, namely between $GMOC^s$ and ACC-RC, between $GMOC^n$ and NADW, and between $GMOC^t$ and ε_m, are 0.73, 0.58, and 0.48, respectively. All these correlations far exceed the 99% significance level (which is approximately 0.12).

***d*, More analysis of GMOC's fingerprints on historic events**

Previous study [43] used a global mean SST (GMSST) residual (GMSSTr) index (a quadratic fit of GMSST is removed) to show the responses of observed GMSST on Mt. Agung (1963), Mt. Chichon (1982) and Mt. Pinatubo (1991) events, three major volcanic eruptions in the second half of the 20th century. They found that the cold GMSSTr anomalies caused by the Agung and Pinatubo volcanic eruptions have a long and profound influence on GMSST since they happen to have occurred at the descending period of a multidecadal GMSST variation. Particularly, the Pinatubo volcanic eruption was the 2nd largest event in the 20th century and the 8th

in history [85], and it had even more profound impacts on global climate compared to the Agung volcanic eruption. Nevertheless, the Chichon volcanic eruption occurred in the ascending period of a GMSST decadal variation and it only produced a short period of cold abnormality for GMSST.

Following that, we first define the global mean sea surface temperature residual (GMSSTr) to identify the SST's fingerprint on prominent volcanic eruption events. The GMSST is an area-weighted mean of 8-year low-passed SST anomalies between 40°S and 60°N and the GMSSTr is obtained by removing the quadratic fit from the GMSST. Then we define a quantity of North Atlantic SST residual (NASSTr) to examine the relationship of NASST anomaly and NADW. The calculation of NASSTr is the same as that of GMSSTr but for only limited in the Northern Atlantic Ocean over the area of 55°–35° W and 45°–65° N.

Figure S15a shows the 8-year low-passed GMSSTr of CDA estimates and the observation which is consistent with Liguori et al. [43]. Affected by the volcanic eruptions of Mt. Agung (1963), Mt. Chichon (1982) and Mt. Pinatubo (1991), the global mean sea surface temperature anomaly (SSTA) showed a significant downward trend. This phenomenon shows consistent manifestations in CDA estimates and OBS.

Figure S16 shows the distributions of SSTA during the periods of 1963–1965, 1982–1985 and 1991–1995 for CESM-CDA and CM2-CDA. Similar with the observation of ERSSTv5 (Extended Reconstructed Sea Surface Temperature version 5) in **Fig.4a–c**, the global SST cooling produced by the eruption of Mt. Agung (1963) mainly occurred in the Southern Hemisphere. In the high-latitude areas of the North Atlantic, the SSTA shows a positive anomaly. This weakens the cooling and sinking of seawater related to local radiation, reduces the thickness of NADW, and leads to a decrease in the corresponding NADW index. However, the SST cooling caused by the eruptions of Mt. Chichon (1982) and Mt. Pinatubo (1991) is mainly in the Atlantic Ocean and the western Pacific Ocean. In the high-latitude waters of the North Atlantic, there are strong negative anomalies. **Fig.S15b** further confirms the different impacts of the three volcanic eruption events on the high-latitude regions of the North Atlantic. The continuous decrease in the NASSTr of Mt. Chichon (1982) and Mt. Pinatubo (1991) corresponds to the continuous increase in NADW, which reaches its maximum around 1997.

Figure S17 shows the CDA-estimated AMMC anomaly distributions during 1963–1965 and 1991–1995 corresponding to Agung and Pinatubo events, respectively. The AMMC anomaly distributions are close to the ERA5 (**Fig.4g&h**). From **Fig.S18**, it can be observed that during the period from 1961 to 1966, the amplitude of the SAM index fluctuated within a wide range. In contrast, between 1980 and 2000, its amplitude is notably small. This variation corresponds to the cooling of the SST in the Southern Ocean during the relevant event. Conversely, the amplitude of the NAO is relatively small from 1961 to 1966 but became considerably larger

382 from 1980 to 2000. Notably, there is a distinct upward trend in the NAO index following the eruptions of
383 Chichon and Pinatubo.

384 **References S1**

385 68. Sun Y, and Zhou TJ. How does El Niño affect the interannual variability of the boreal summer Hadley
386 circulation? *J Clim*, 2014, **27**, 2622–2642. https://doi.org/10.1175/JCLI-D-13-00277.1
387 69. Chang Y, Zhang S, Rosati A, Delworth T, and Stern W. An assessment of oceanic variability for 1960–
388 2010 from the GFDL ensemble coupled data assimilation. *Clim Dyn*, 2013, **40**, 775–803.
389 https://doi.org/10.1007/s00382-012-1412-2
390 70. Huang RX, Wang W, and Liu LL. Decadal variability of wind-energy input to the world ocean. *Deep*
391 *Sea Res. Part II: Topical Studies in Oceanography*, 2006, **53**(1), 31–41.
392 https://doi.org/10.1016/j.dsr2.2005.11.001
393 71. Cronin MF, Gentemann CL, Edson J, et al. Air-sea fluxes with a focus on heat and momentum. *Front*
394 *Mar Sci*, 2019, **6**, 430. doi:10.3389/fmars.2019.00430
395 72. Buckley MW, and Marshall J. Observations, inferences, and mechanisms of Atlantic meridional
396 overturning circulation variability: A review. *Rev Geo*, 2016, **54**, 5–63.
397 https://doi.org/10.1002/2015RG000493
398 73. Stommel H. Thermohaline convection with two stable regimes of flow. *Tellus*, 1961, **13**(2), 224–230.
399 https://doi.org/10.1111/j.2153-3490.1961.tb00079.x
400 74. Manabe S. Climate and the ocean circulation: I. The atmospheric circulation and the hydrology of the
401 Earth's surface. *Mon Wea Rev*, 1969, **97**(11), 739–774. https://doi.org/10.1175/1520-
402 0493(1969)097<0739:CATOC>2.3.CO;2
403 75. Charney JG, and Drazin PG. Propagation of planetery scale disturbances from the lower into the upper
404 atmosphere. *J Geophys Res*, 1961, **66**, 83–109. https://doi.org/10.1029/JZ066i001p00083
405 76. Zhang, S., Xu, S., Fu, H., et al. Toward Earth system modeling with resolved clouds and ocean submesoscales
406 on heterogeneous many-core HPCs. Natl. Sci. Rev., 10, nwad069 (2023). https://doi:10.1093/nsr/nwad069
407 77. Zhang, S. & Rosati, A. An inflated ensemble filter for ocean data assimilation with a biased coupled GCM.
408 Mon. Wea. Rev., 138, 3905–3931 (2010). DOI: 10.1175/2010MWR3326.1
409 78. Griffies SM, Danabasoglu G, Durack PJ, et al. OMIP contribution to CMIP6: experimental and
410 diagnostic protocol for the physical component of the Ocean Model Intercomparison Project. *Geo Mod*
411 *Dev*, 2016, **9**(9), 3231–3296. https://doi.org/10.1175/1520-0469(1950)007<0080:OTWDOC>2.0.CO;2
412 79. Jayne SR, Roemmich D, Zilberman N, Riser SC, Johnson KS, Johnson GC, and Piotrowicz SR. The
413 Argo program: present and future. *Oceanography*, 2017, **30**(3), 18–28.
414 https://doi.org/10.5670/oceanog.2017.213
415 80. Donlon CJ, Martin M, Stark J, Robert-Jones J, Fiedler E, and Wimmer W. The operational sea surface
416 temperature and sea ice analysis (OSTIA) system. *Remote Sens Environ*, 2012, **116**, 140–158.
417 https://doi.org/10.1016/j.rse.2010.10.017

81. Abraham JP, Baringer M, Bindoff NL, et al. A review of global ocean temperature observations: Implications for ocean heat content estimates and climate change. *Rev Geo*, 2013, **51**(3), 450–483. https://doi.org/10.1002/rog.20022
82. Hurrell JW, and Deser C. North Atlantic climate variability: The role of the North Atlantic Oscillation. *J Mar Syst*, 2009, **78** (1), 28–41. https://doi.org/10.1016/j.jmarsys.2009.11.002
83. Trenberth K-E, and Hoar T-J. The 1990-1995 El Nino-Southern Oscillation event longest on record. *Geo Res Lett*, 1996, **23**, 57–60. https://doi.org/10.1029/95GL03602
84. Marshall GJ. Trends in the Southern Annular Mode from observations and reanalyses. *J Clim*, 2003, **16**, 4134–4143. https://doi.org/10.1175/1520-0442(2003)016<4134:TITSAM>2.0.CO;2
85. Ghose, T. The 12 biggest volcanic eruptions in recorded history. Live Science, Future US, Inc. Full 7th Floor, 130 West 42nd Street, New York, NY 10036 (2023). https://www.livescience.com/planet-earth/volcanos/the-12-biggest-volcanic-eruptions-in-recorded-history.

Figs. S1-S18:

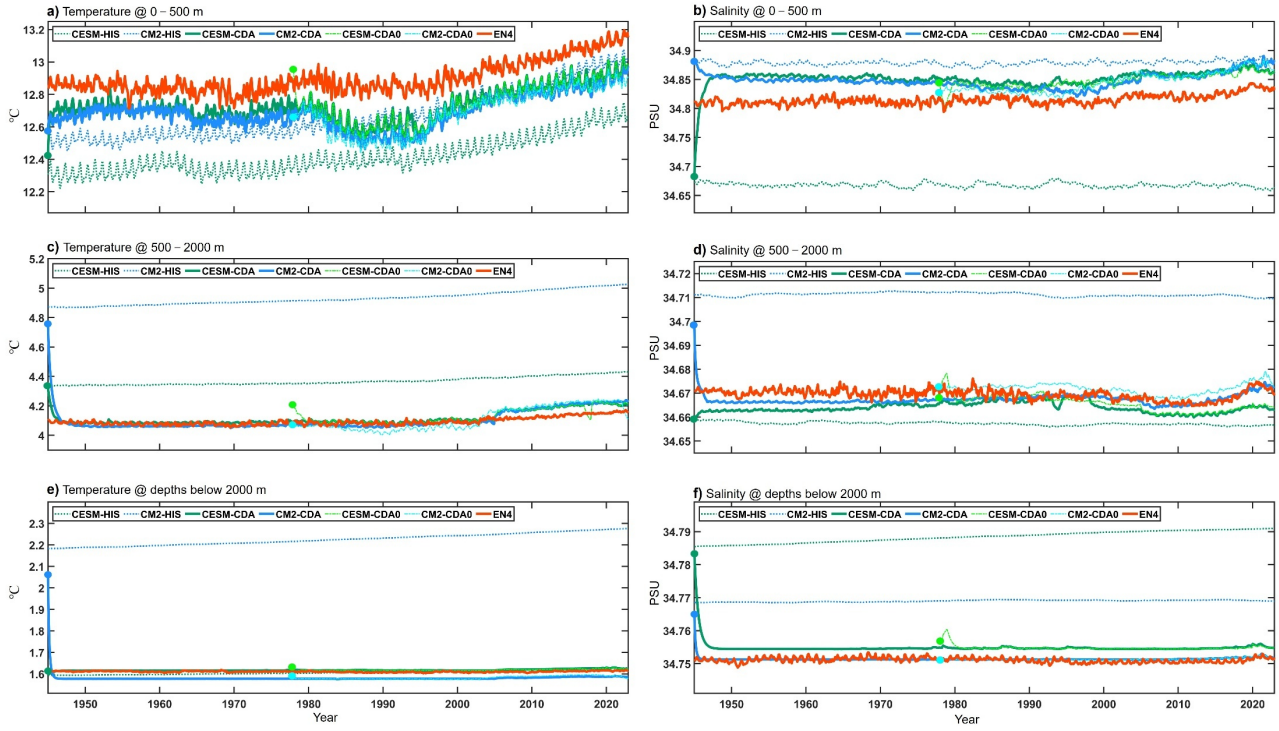

Fig. S1 | Convergent ocean temperature and salinity in coupled data assimilation (CDA) estimates. a–b) Time series of **a**) mean temperature (unit: °C) and **b**) salinity (unit: PSU) over the area 60° S–60° N at 0–500 m ocean depth. The dashed light-green and light-blue lines represent other CDA experiments (CESM-CDA0 and CM2-CDA0) for the period 1978–2022 [30]. The restart initial condition (denoted by a light-green dot) of CESM-CDA0 is the coupled model state at 00:00 UTC on 01-01-1978 of the historical model simulation running from 01-01-1869. The restart initial condition (denoted by a light-blue dot) of CM2-CDA0 is the previous assimilation coupled state at 00:00 UTC on 01-01-1978 [69]. **c–d**) Same as panels **a–b** but for 500–2000 m ocean depth. **e–f**) Same as panels **a–b** but for the ocean depths below 2000 m.

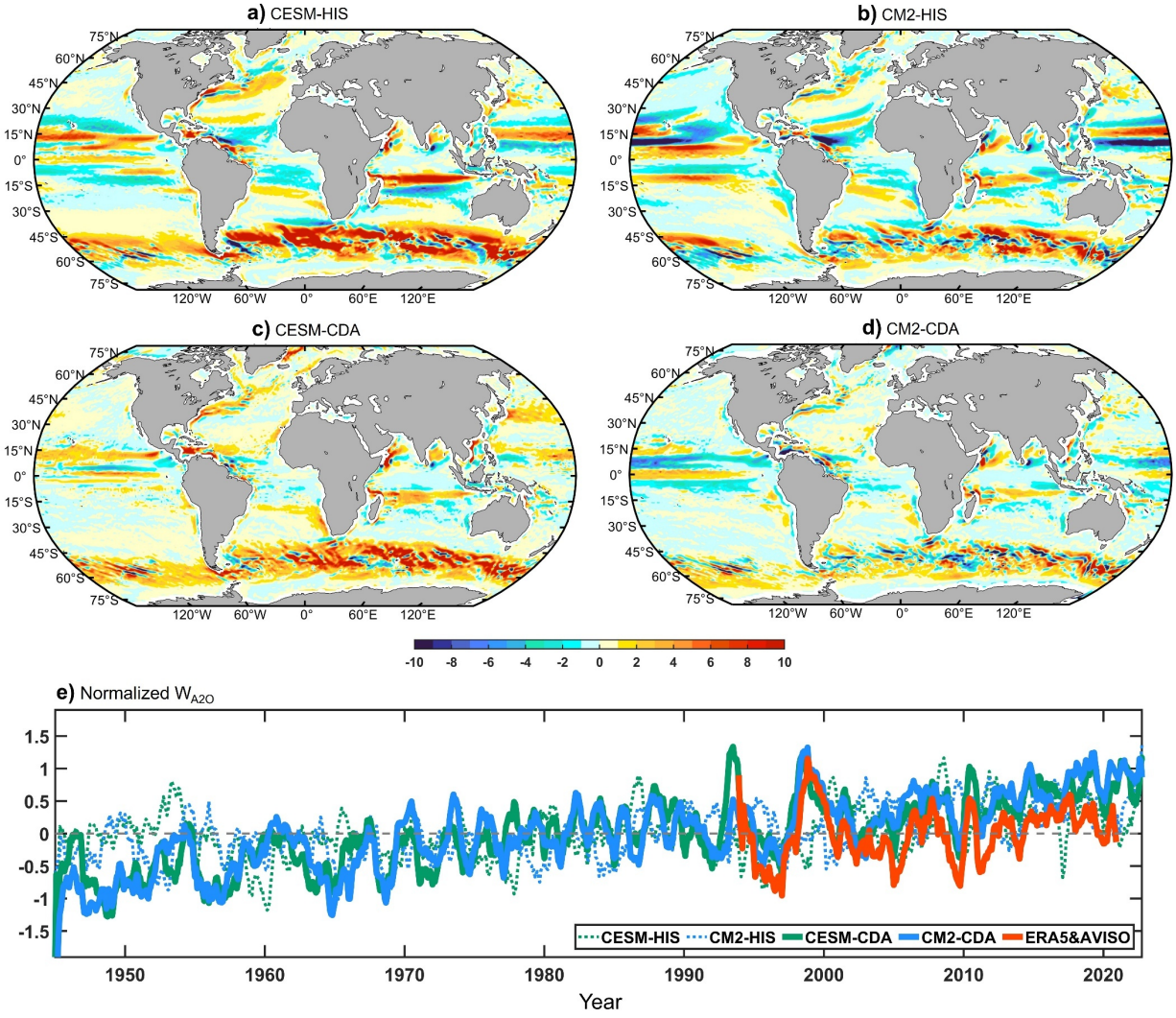

Fig. S2 | Atmospheric work exerted on the oceans (W_{A2O}). a–d) Error distributions of W_{A2O} for CESM-HIS, CM2-HIS, CESM-CDA, and CM2-CDA, respectively, against the observed product derived from ERA5 and AVISO over the period 1993–2020 (unit: mW/m^2). **e**) Normalized global mean time series of W_{A2O} in CESM-HIS (green dotted line), CM2-HIS (blue dotted line), CESM-CDA (green solid line), CM2-CDA (blue solid line), and the observed product (red solid line).

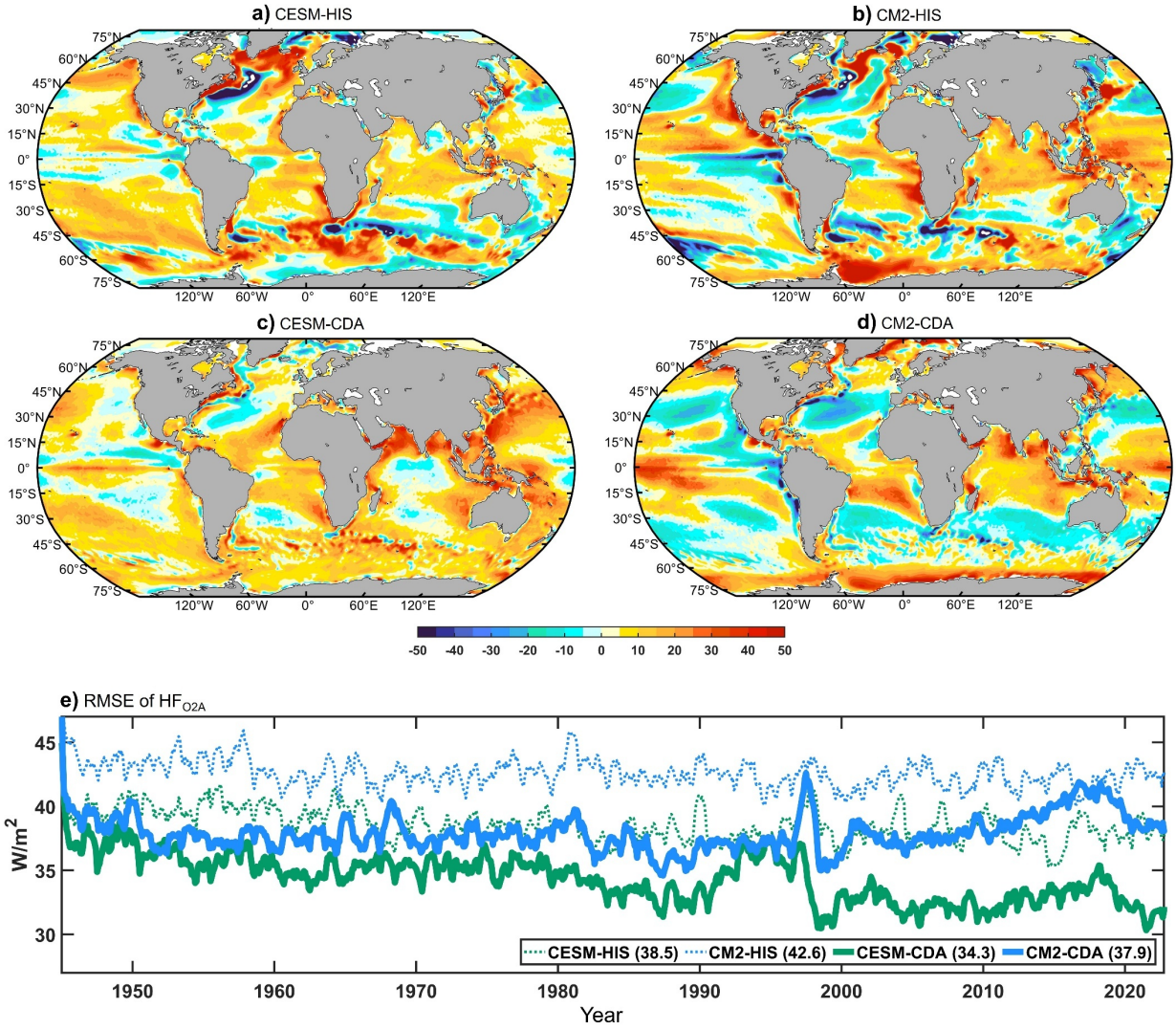

Fig. S3 | Convergent oceanic heat flux to the atmosphere (HF_{O2A}) in coupled data assimilation (CDA) estimates. a–d) Error distributions of HF_{O2A} in CESM-HIS, CM2-HIS, CESM-CDA, and CM2-CDA, respectively, verified against ERA5. **e**) Time series of HF_{O2A} root-mean-square error (RMSE) against ERA5 in CESM-HIS (green dotted line), CM2-HIS (blue dotted line), CESM-CDA (green solid line), and CM2-CDA (blue solid line) (unit: W/m^2). The average value for each line is indicated in the figure key.

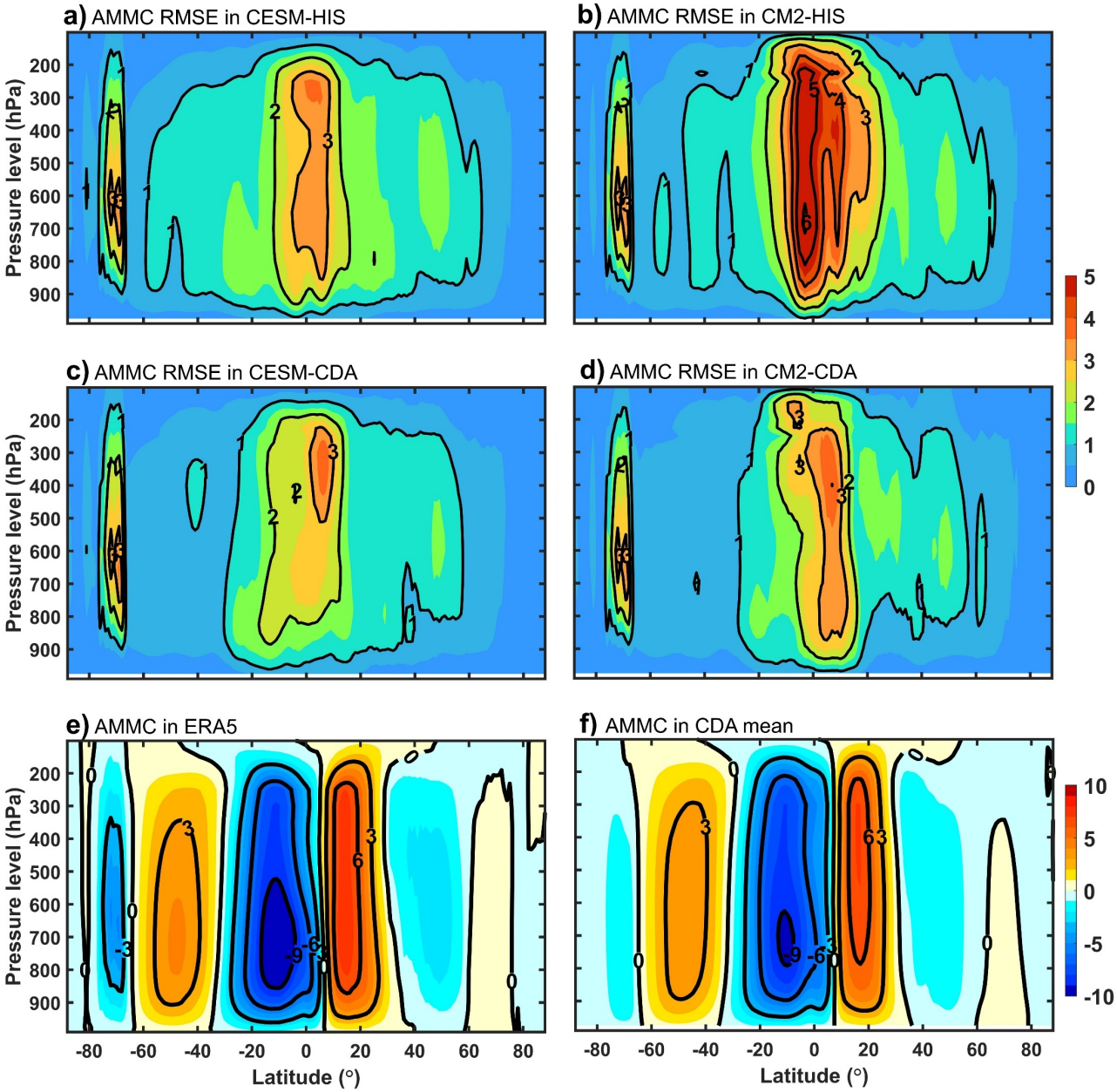

Fig. S4 | Convergent atmospheric mean meridional circulation (AMMC) mean state in coupled data assimilation (CDA) estimates. a–d) Root-mean-square error (RMSE) distributions of AMMC for the model simulations CESM-HIS and CM2-HIS, and the CDA results CESM-CDA and CM2-CDA, verified against ERA5. **e–f**) Mean states of AMMC in ERA5 and CDA mean, respectively (unit: 10^{10} kg/s).

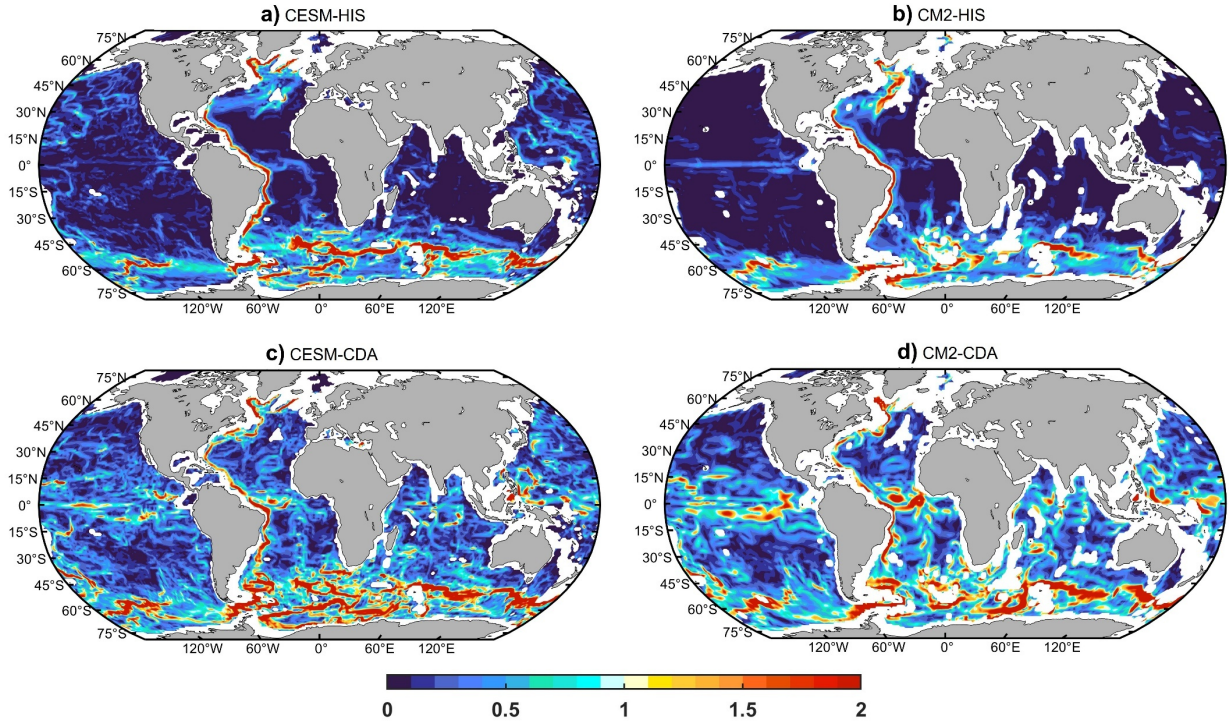

458

459 **Fig. S5 | Convergent deep-ocean current velocities in coupled data assimilation (CDA) estimates. a–d)**
460 Temporal mean distributions of 2500–5000 m ocean current velocities (unit: cm/s) in CESM-HIS, CM2-HIS,
461 CESM-CDA, and CM2-CDA, respectively.

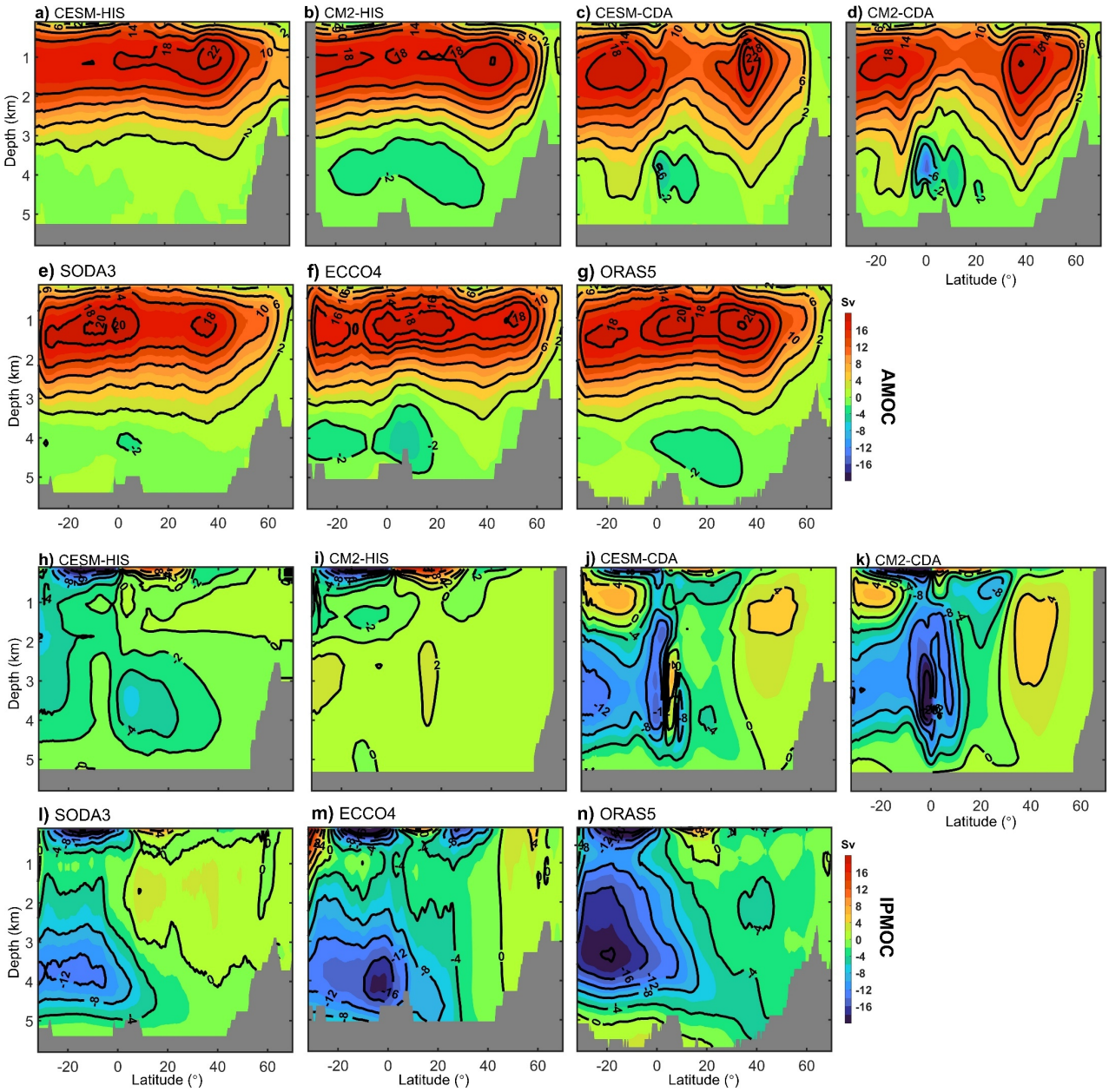

Fig. S6 | Convergent Atlantic and Indo-Pacific meridional overturning circulations (AMOC and IPMOC) in coupled data assimilation (CDA) estimates. a–g) Temporal mean AMOC (unit: Sv) in CESM-HIS, CM2-HIS, CESM-CDA, CM2-CDA, SODA3, ECCO4, and ORAS5, respectively. **h–n**) Same as **a–g**) but for IPMOC.

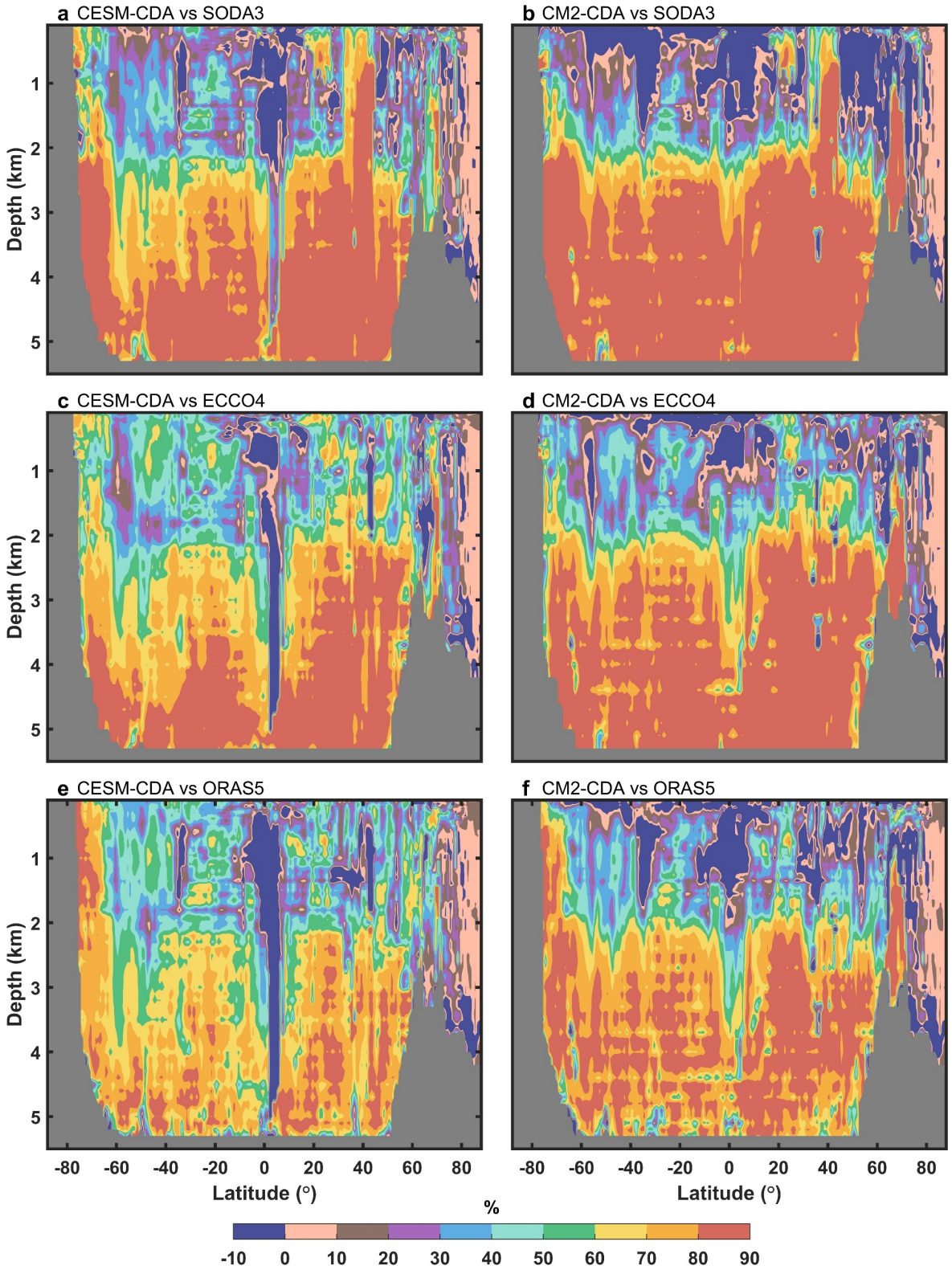

Fig. S7 | Coherent ocean stratification in coupled data assimilation (CDA) estimates. a–f) Latitudinal distributions of root-mean-square error (RMSE) reduction rates (unit: %) for potential density compared with **a–b)** SODA3, **c–d)** ECCO4, and **e–f)** ORAS5 in CESM-CDA (left panels) and CM2-CDA (right panels), verified against the WOA18.

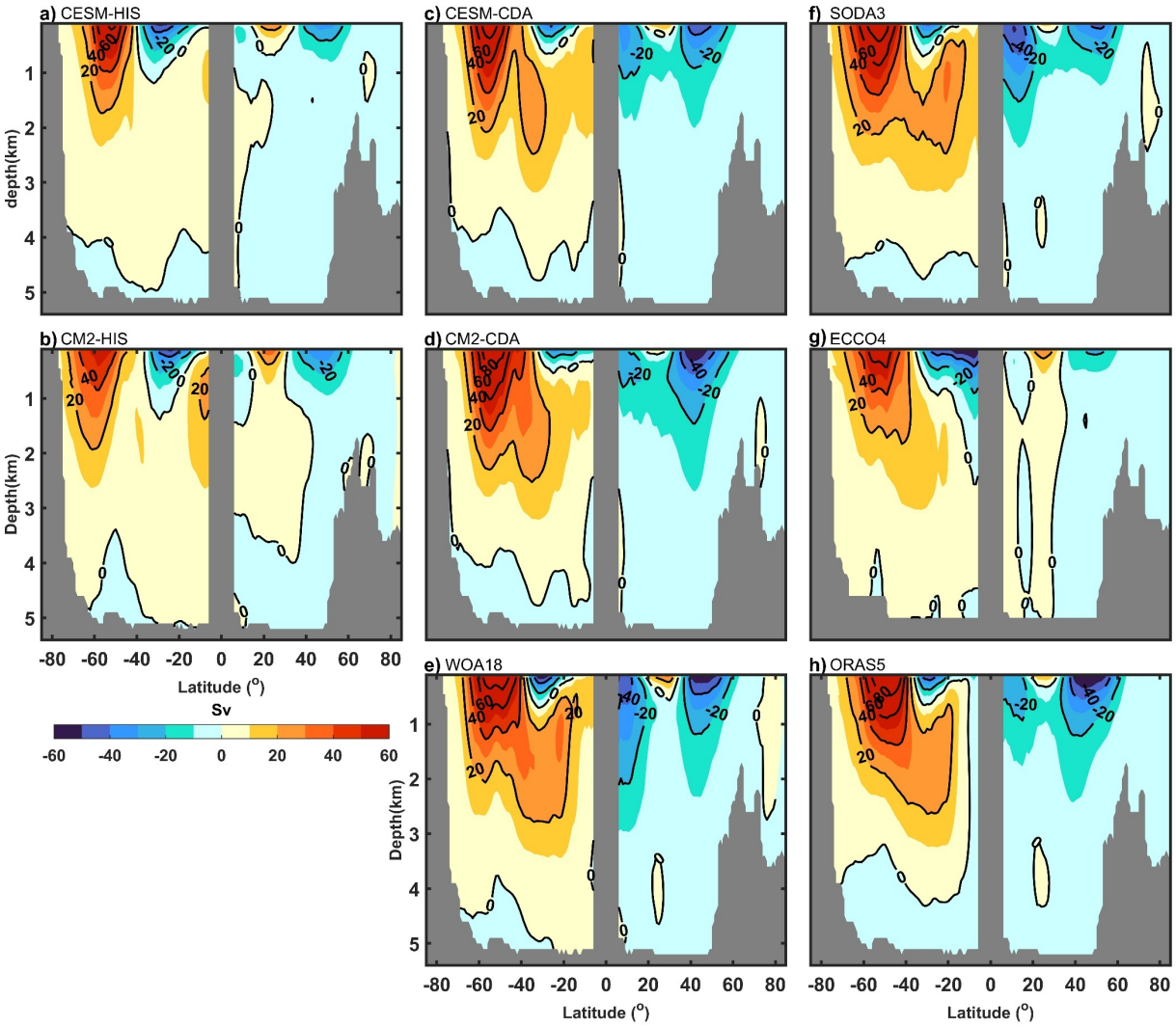

Fig. S8 | Geostrophic global meridional overturning circulation (GMOC) mean states of model simulations and assimilation products. a–h) Geostrophic GMOC mean states in CESM-HIS, CM2-HIS, CESM-CDA, CM2-CDA, WOA18, SODA3, ECCO4, and ORAS5, respectively.

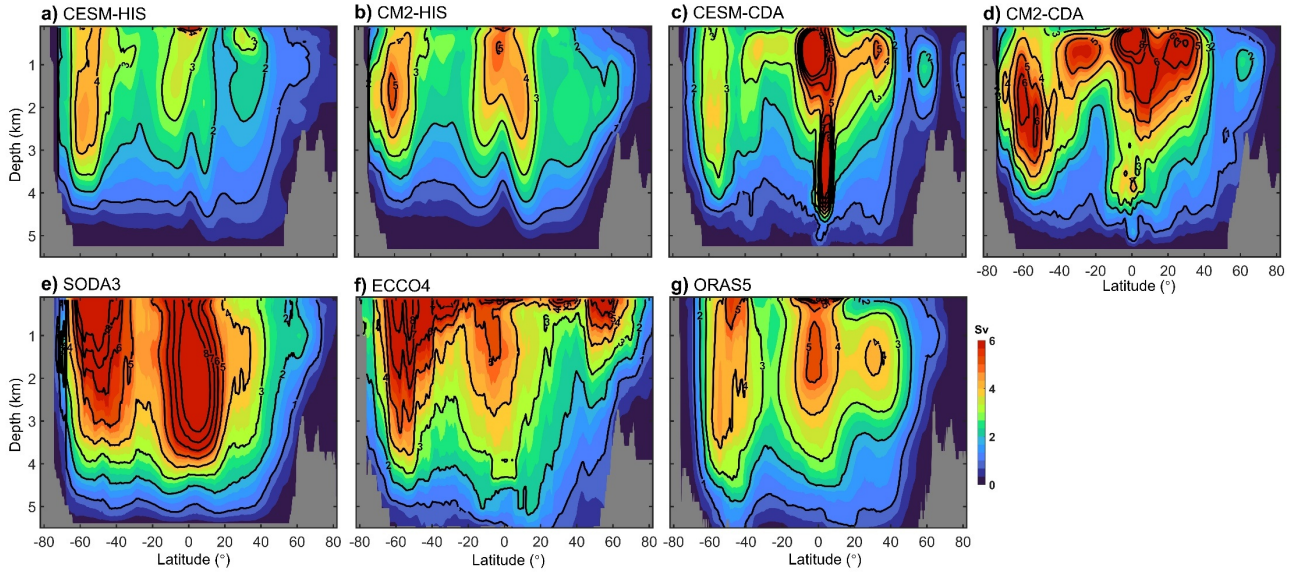

476

477 **Fig. S9 | Distributions of global meridional overturning circulation (GMOC) standard deviations in model**
478 **simulations and assimilation products. a–g**) Standard deviations of GMOC stream functions (unit: Sv) in CESM-
479 HIS, CM2-HIS, CESM-CDA, CM2-CDA, SODA3, ECCO4, and ORAS5, respectively.

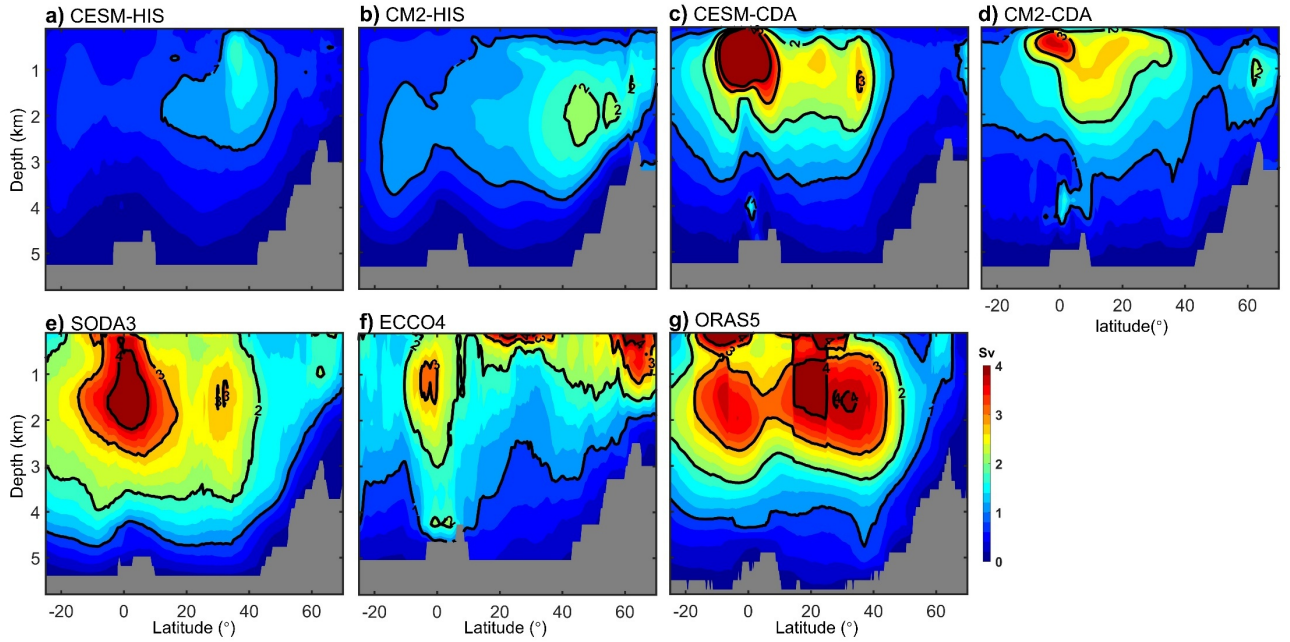

480

481 **Fig. S10 | Same as Fig. S9 but for Atlantic meridional overturning circulation (AMOC).**

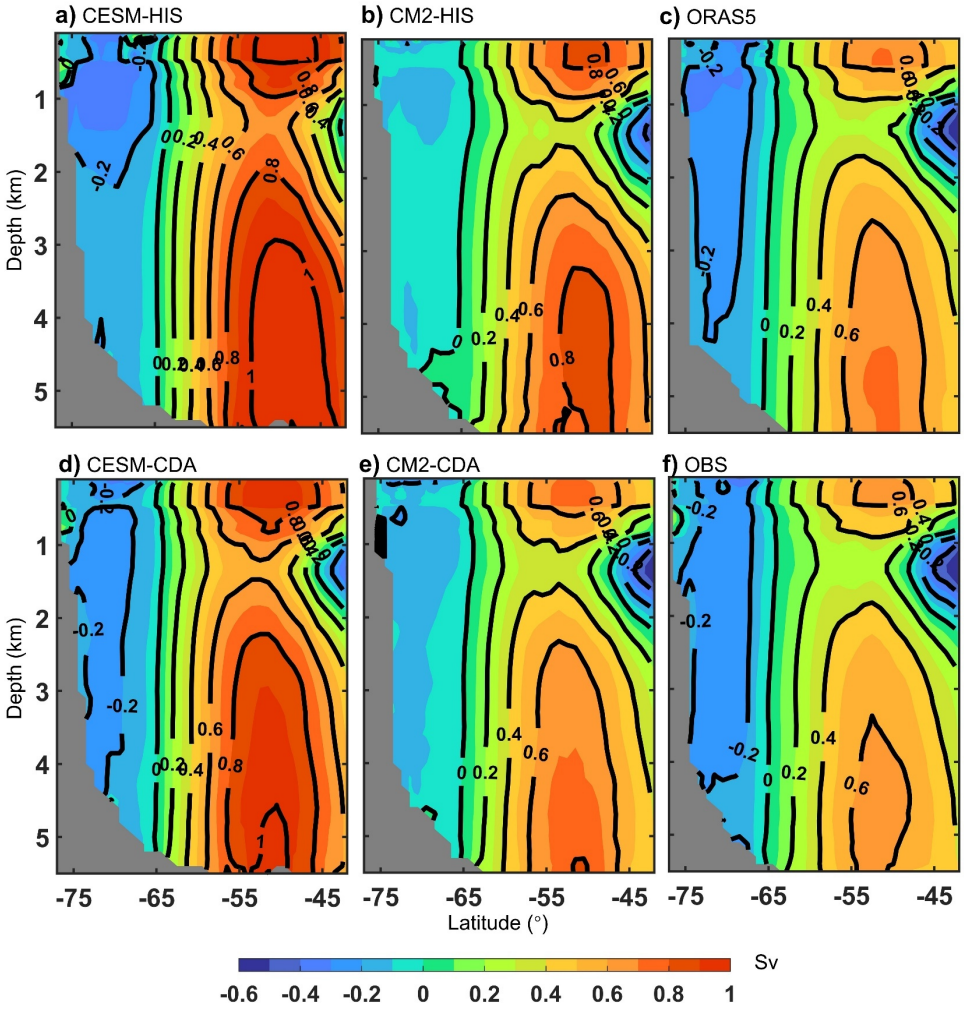

Fig. S11 | Coupled data assimilation (CDA)-estimated Antarctic Circumpolar Current residual circulation (ACC-RC). a–f) Mean states of ACC-RC stream functions for **a**) CESM-HIS, **b**) CM2-HIS, **c**) ORAS5, **d**) CESM-CDA, **e**) CM2-CDA, and **f**) observational result (calculated from EN4 and ERA5).

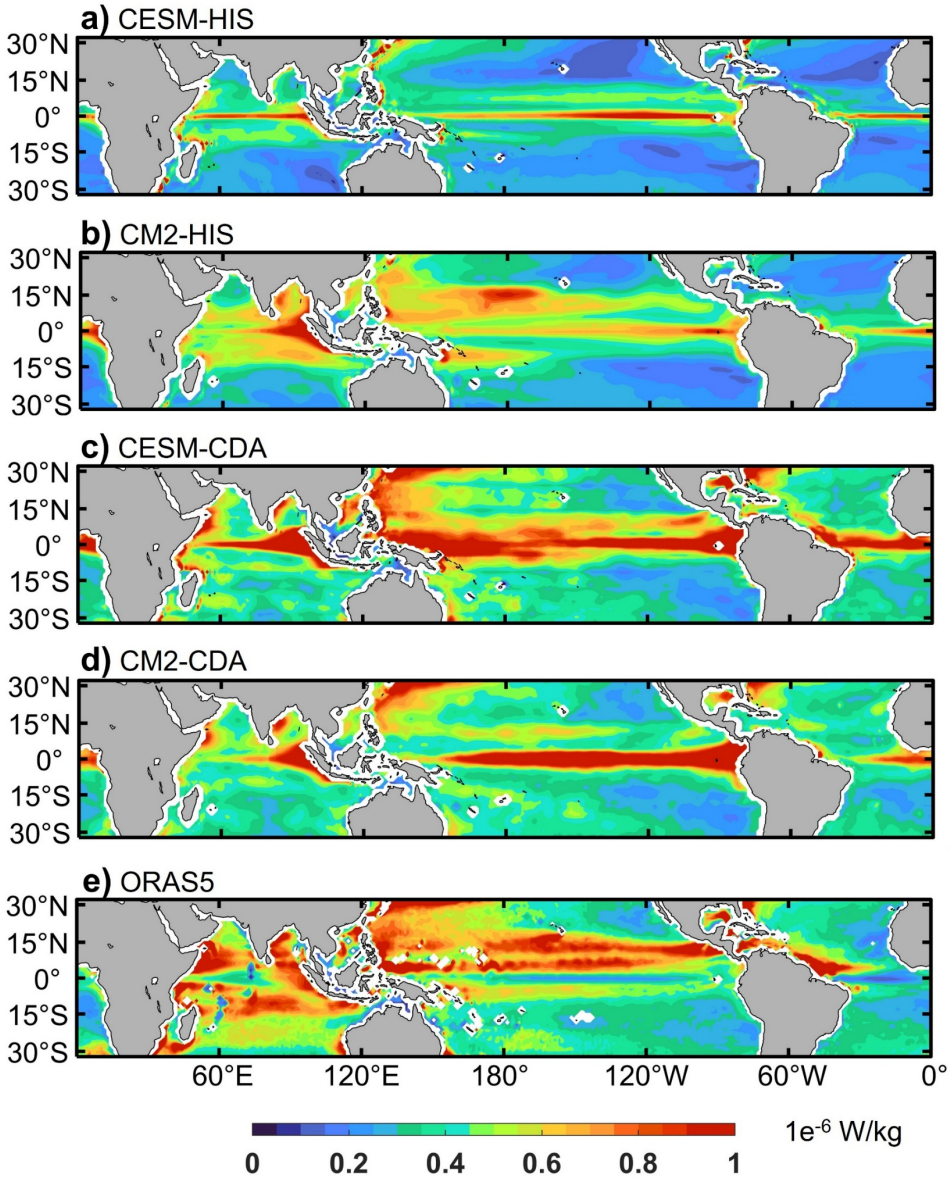

Fig. S12 | Coupled data assimilation (CDA-)estimated tropical diffusive mixing. a–e, Temporal mean distributions of tropical (30° S–30° N) kinetic energy dissipation rate [ε_m] (unit: $1e^{-6}$ W/kg) in **a**) CESM-HIS, **b**) CM2-HIS, **c**) CESM-CDA, **d**) CM2-CDA, and **e**) ORAS5 ocean reanalysis.

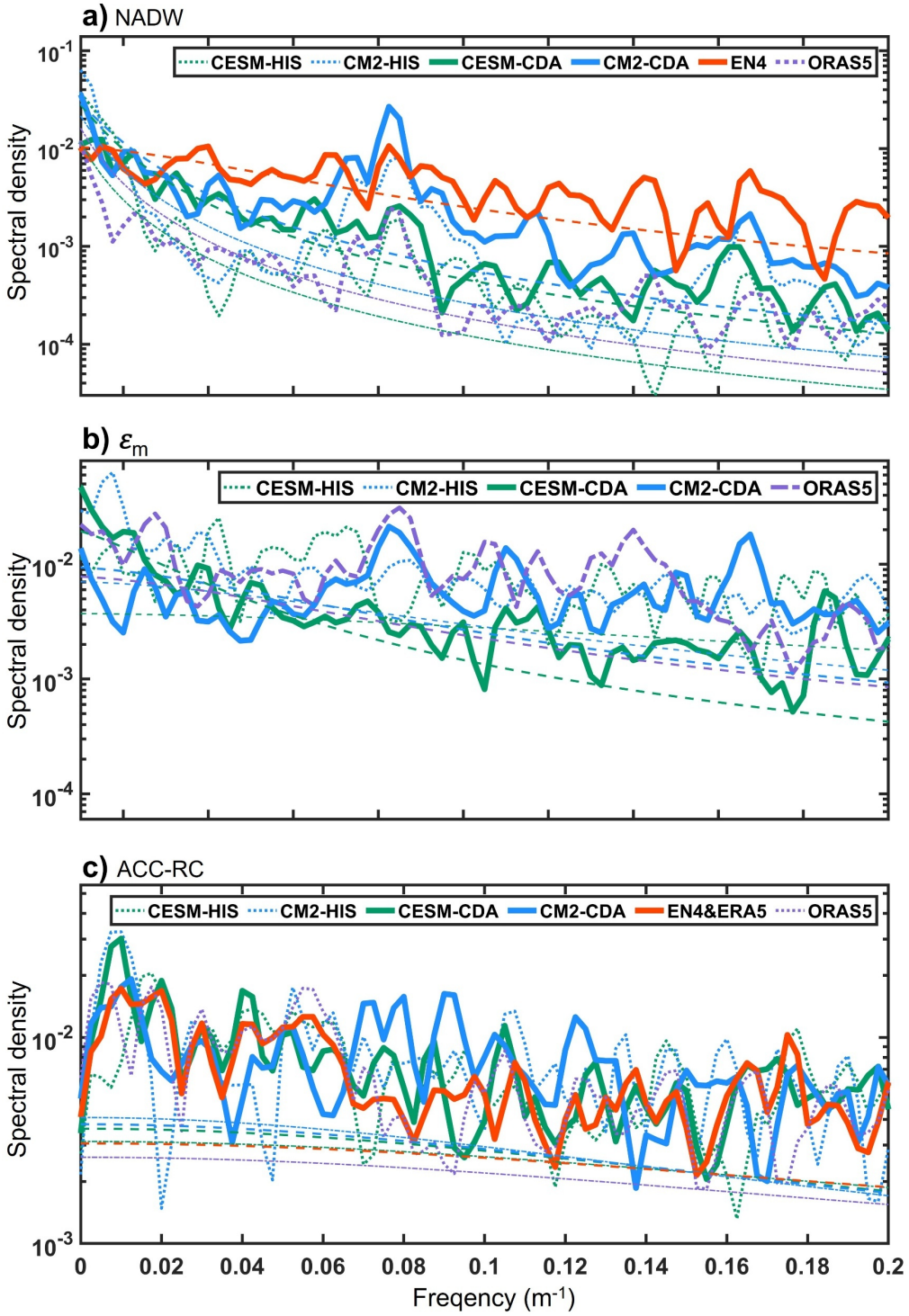

490

491 **Fig. S13 |** Spectrogram of **a**) North Atlantic Deep Water (NADW), **b**) tropical diffusive mixing (ε_m), and **c**)
492 Antarctic Circumpolar Current residual circulation (ACC-RC).

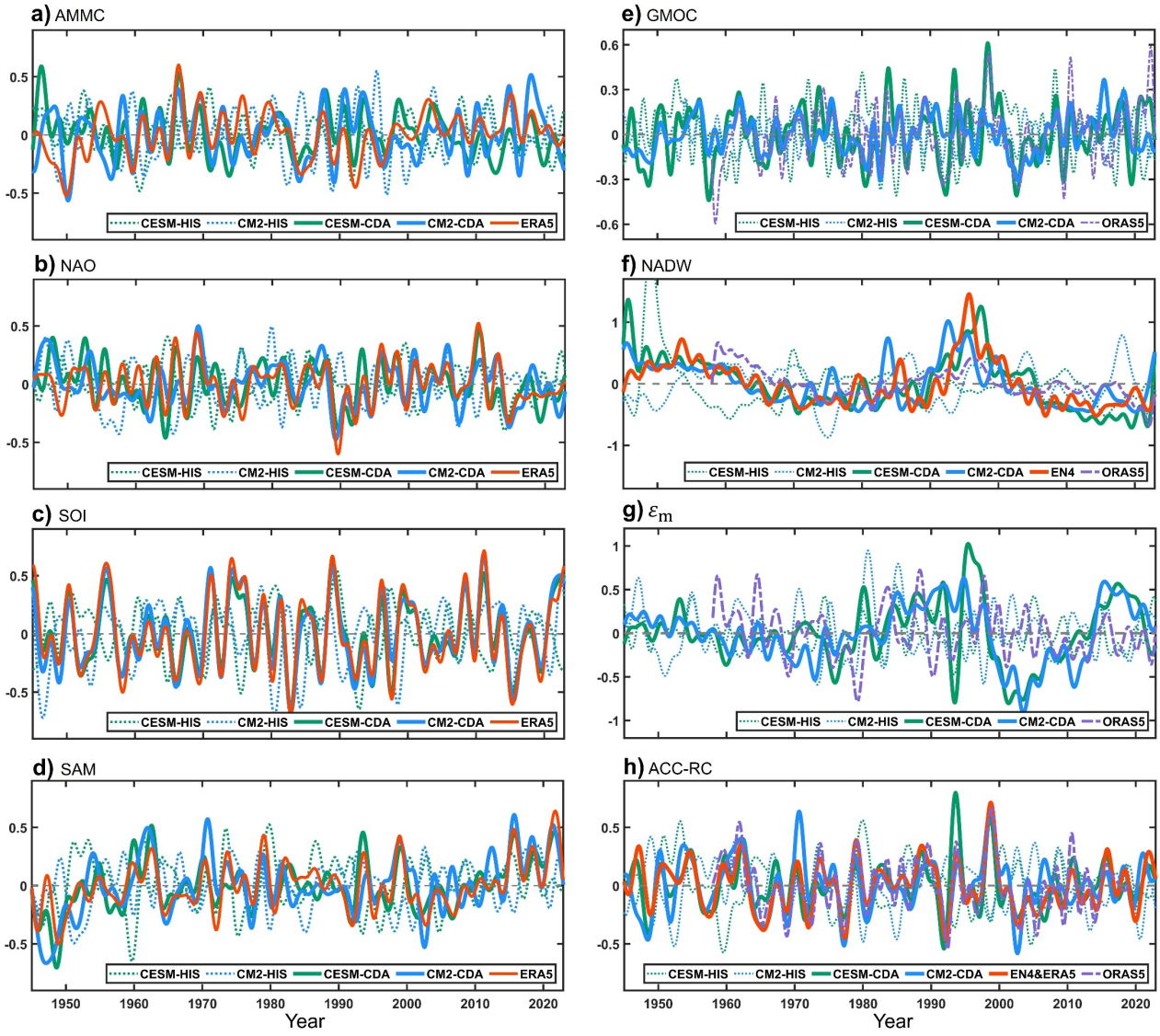

493

494 **Fig. S14 | Convergent variability of various components of atmospheric mean meridional circulation (AMMC)**
495 **and global meridional overturning circulation (GMOC) in coupled data assimilation (CDA) estimates. a–d)**
496 The normalized 1–20-yr band-pass filtered time series of **a**) AMMC, **b**) North Atlantic oscillation (NAO), **c**)
497 Southern Oscillation Index (SOI), and **d**) Southern Annular Mode (SAM) indices, respectively. **e–h**) The normalized
498 1–20-yr band-pass filtered time series of **e**) GMOC, **f**) North Atlantic Deep Water (NADW), **g**) tropical diffusive
499 mixing (ε_m), and **h**) Antarctic Circumpolar Current residual circulation (ACC-RC), respectively.

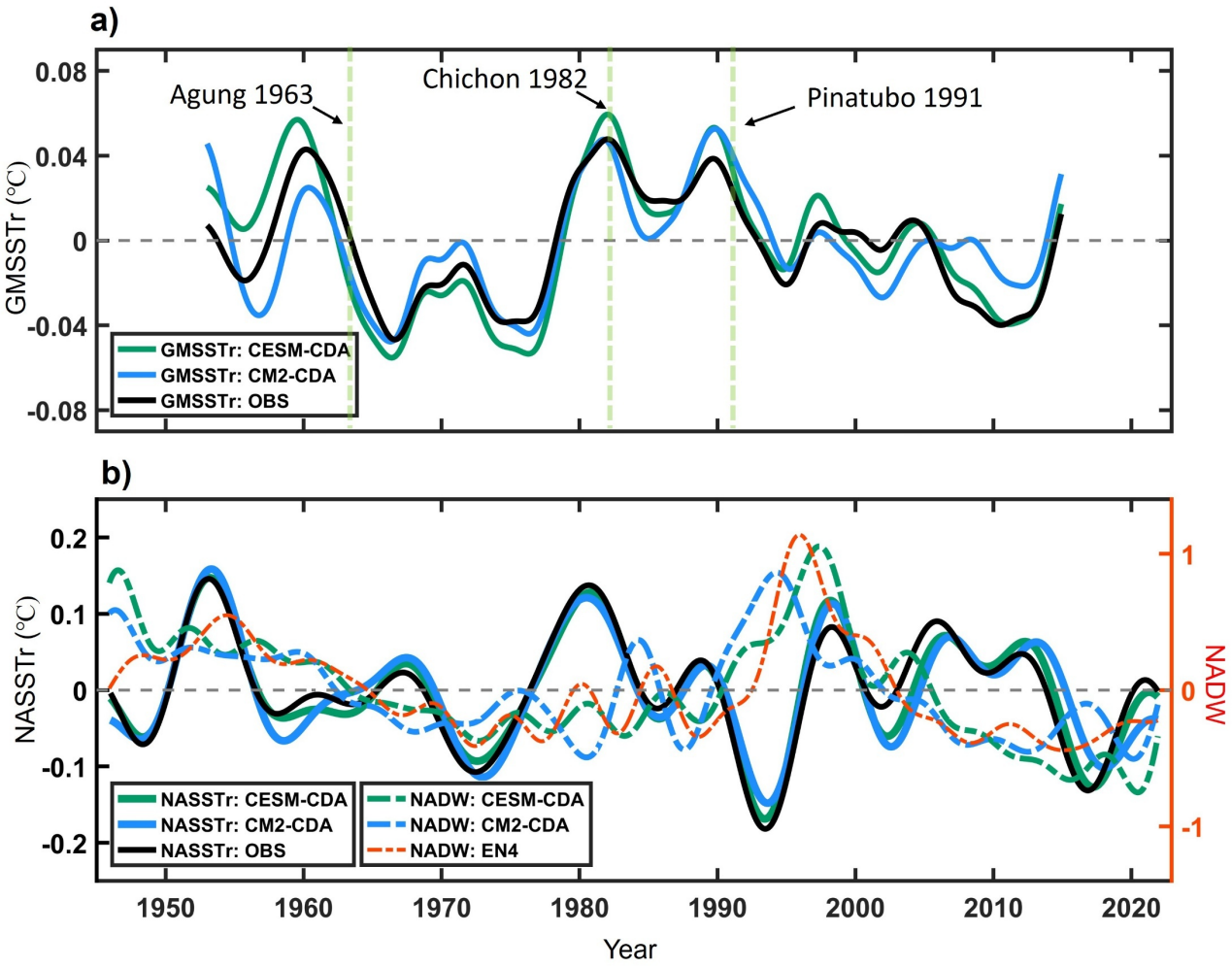

Fig. S15 | Decadal variability of global and North Atlantic mean sea surface temperature (SST) anomaly residual (GMSSTr and NASSTr) and North Atlantic Deep Water (NADW) in coupled data assimilation (CDA) estimates. a) Time series of GMSSTr for CDA estimates CESM-CDA (green-solid) and CM2-CDA (blue-solid) as well as observation (OBS, black-solid) (°C). The GMSSTr is obtained by removing the quadratic fit from the GASST (computed from 8-year low-passed SST). The GMSST is defined as area-weighted mean SST between 40°S and 60°N and anomalies are relative to the 1980–2010 mean [43]. **b**) Time series of 5–20-yr band-pass filtering NASSTr for observation (black-solid, °C) and 2–20-yr band-pass filtering normalized NADW for CESM-CDA (green-dash) and CM2-CDA (blue-dash). The NASSTr is obtained by removing the quadratic fit from the NASST, which is computed from 1-year low-passed SSTA over the area of 55°–35° W and 45°–65° N.

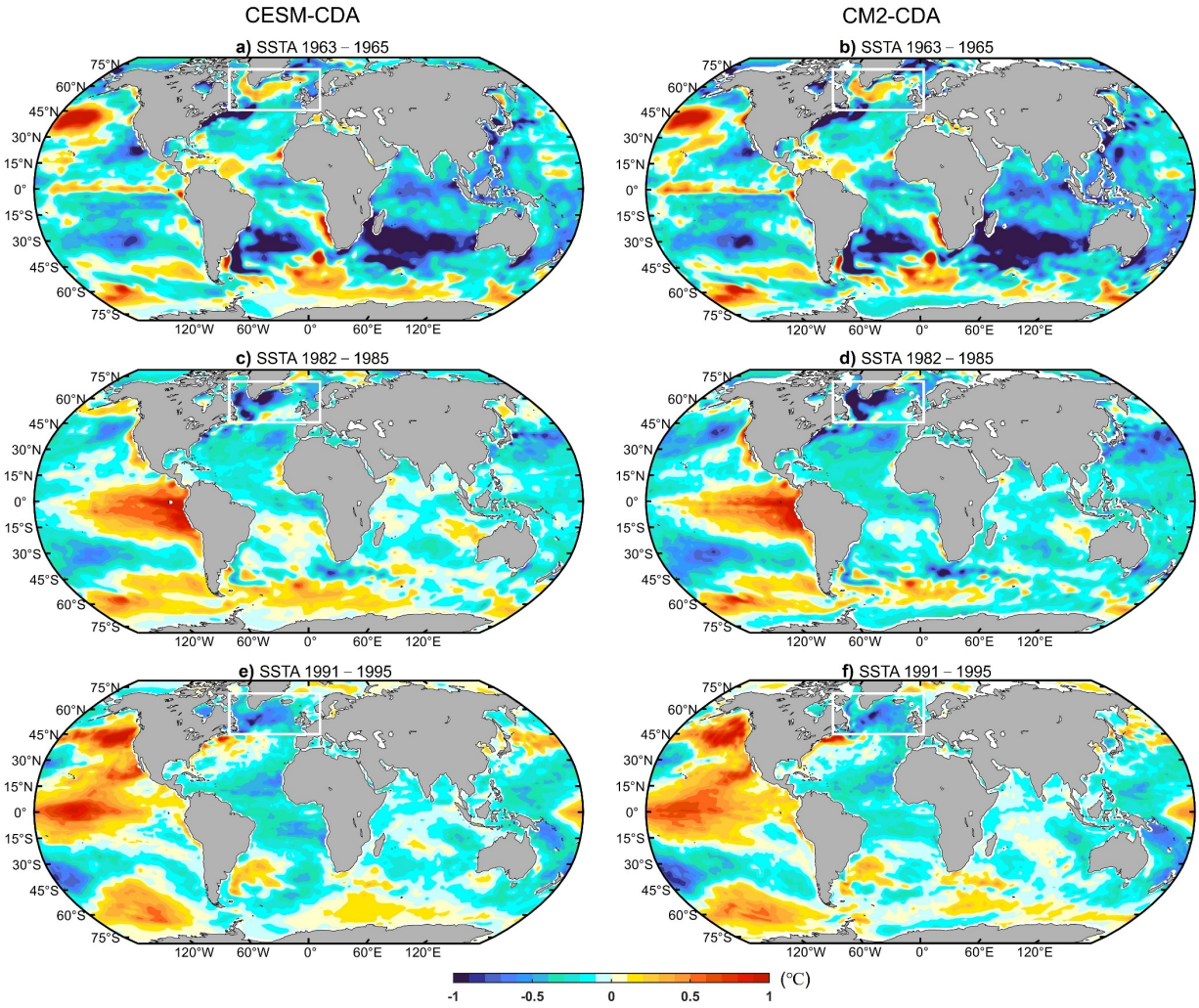

510

511 **Fig. S16 | Temperature response after major volcanic events. a–b**) Distribution of sea surface temperature (SST)
512 anomaly (SSTA) during the period of 1963–1966 for **a**) CESM-CDA and **b**) CM2-CDA. **c–d**) Same as **a–b**) but for
513 period 1982–1985. **e–f**) Same as **a–b**) but for period 1991–1995.

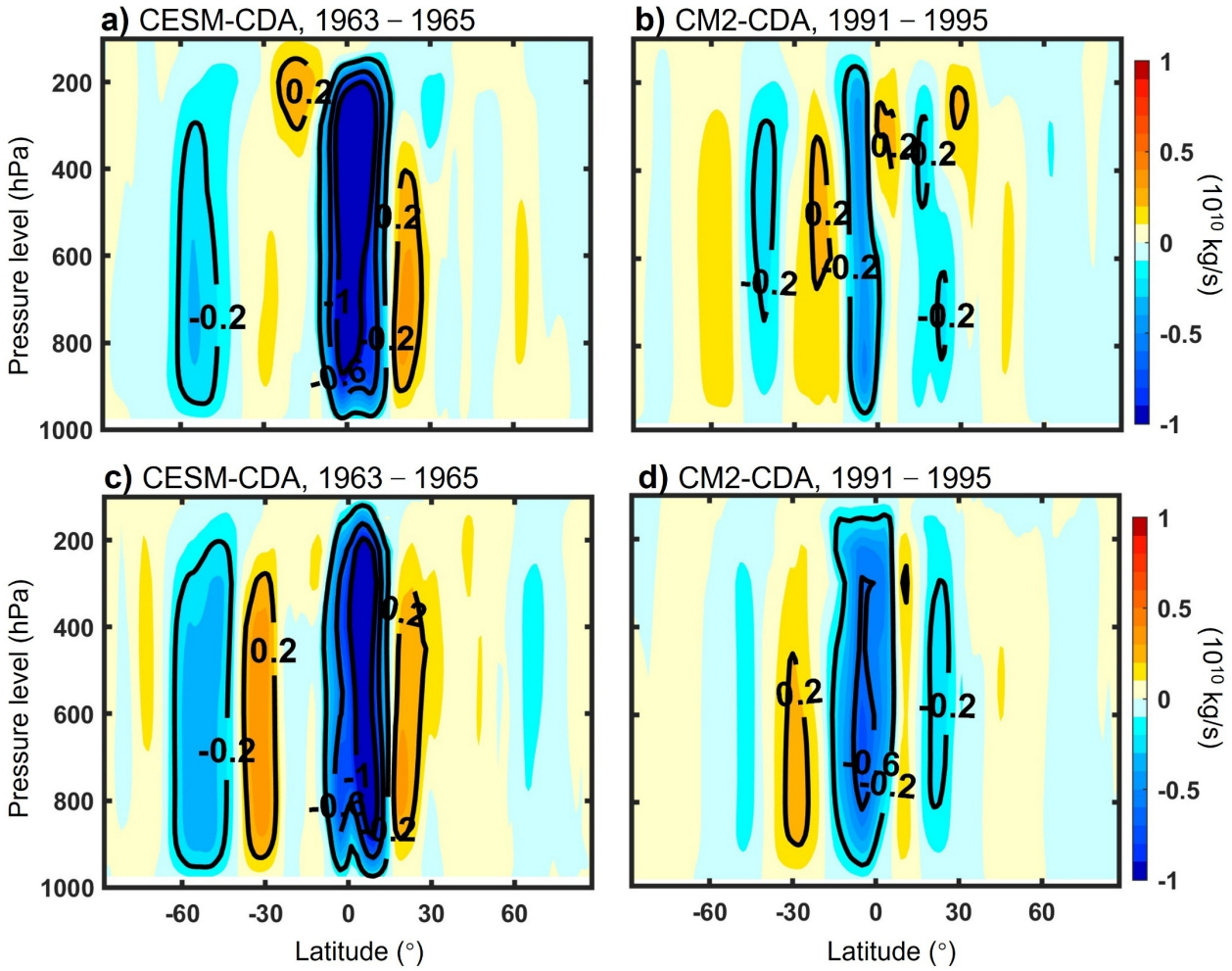

514

515 **Fig. S17 |** Atmospheric meridional mean meridional circulation (AMMC) anomaly distributions during (left panels)
516 1963–1965 and (right panels) 1991–1995 for **a**–**b**) CESM-CDA and **c**–**d**) CM2-CDA.

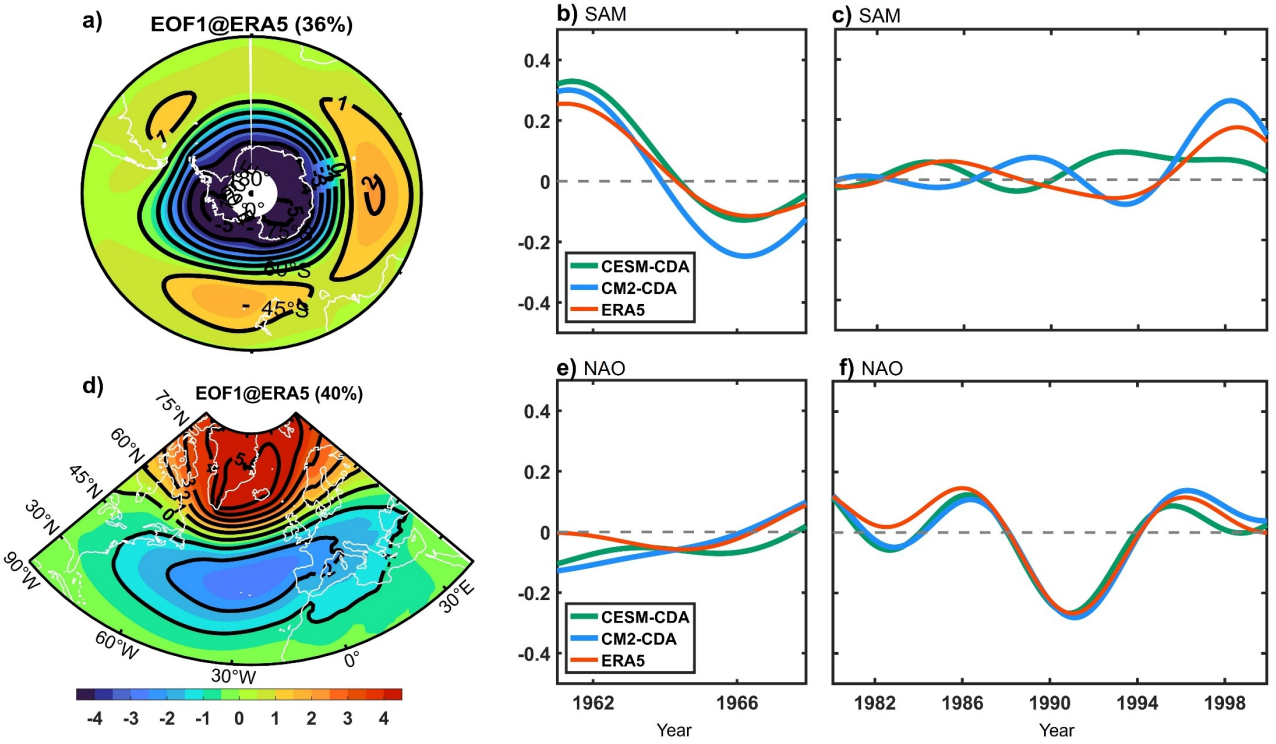

Fig. S18 | a) The leading Empirical Orthogonal Function (EOF) of sea level pressure (SLP) anomalies over the Southern Ocean. **b–c**) Time series of 5–20-yr band-pass filtering Southern Annular Mode (SAM) during periods of **b**) Mt. Agung (1963), **c**) Mt. Chichon (1982) and Mt. Pinatubo (1991) volcanic eruptions. **d–f**) Same as **a–c**) but for the Atlantic and the North Atlantic Oscillation (NAO).

Tables S1-S3:

Table S1. List of acronyms.

Acronym	Full name	Description/Definition/Role in this study
ACC	Antarctic Circumpolar Current	An ocean circulation system around the Antarctic
ACC-RC	Residual circulation of the Antarctic Circumpolar Current system	A circulation to reflect the balance between direct Ekman effects and counteracting influences of eddy-induced transport in ACC.
AM2.1	Atmosphere Model version 2.1	Atmospheric component model of CM2
AMMC	Atmospheric mean meridional circulation	The atmospheric vertical circulation in y-z plane
AMOC	Atlantic meridional overturning circulation	An important branch of ocean meridional overturning circulation in the Atlantic
Argo	Array for real-time geostrophic oceanography	An international program that deploys a global array of free-floating profiling floats to measure upper 2000 ocean temperature and salinity
CAM5	Community Atmosphere Model version 5	Atmospheric component of CESM
CDA	Coupled data assimilation	A data constraint approach using coupled models
CESM	Community Earth System Model developed at the National Center for Atmospheric Research	One of coupled models used in this study as assimilation model
CESM-CDA	CDA system/experiment using CESM	CDA system/experiment by applying multiscale CDA algorithm to CESM
CESM-CDA0	The formal version of CDA experiment using CESM	Experiment evaluated in Jiang et al. (2024)
CESM-HIS	Historical simulation experiment of CESM	CESM control run without data assimilation
CICE4	Community Ice Code version 4	An ice component model of CESM
CLM4	Community Land Model version 4	A land component model of CESM
CM2	The second generation of Coupled Climate Model developed at the Geophysical Fluid Dynamics Laboratory	One of coupled models used in this study as assimilation model
CM2-CDA	CDA system/experiment using CM2	CDA system/experiment by applying multiscale CDA algorithm to CM2
CM2-CDA0	The formal version of CDA experiment using CM2	Experiment evaluated in Jiang et al. (2024)
CM2-HIS	Historical simulation experiment of CM2	CM2 control run without data assimilation
ECCO4	Estimating the Circulation and Climate of the Ocean version 4 release 3	One of 3 ocean reanalysis products used in this study as references
EN4	Version 4 of global ocean objective analysis dataset of observations combining from two European Union projects: ENACT (Enhanced Ocean Data Assimilation and Climate Prediction; http://www.ecmwf.int/research/EU_projects/ENACT/index.html) and ENSEMBLES (http://ensembles-eu.metoffice.com/index.html).	The subsurface temperature and salinity observation dataset used in this study to evaluate CDA results
EOF	Empirical Orthogonal Function	An analysis method; Each EOF represents a spatial pattern.
ECMWF	European Centre for Medium-Range Weather Forecasts	An institution on numerical weather and climate prediction
ERA5	The fifth-generation ECMWF reanalysis starting from 1940	Atmospheric reanalysis products used for CDA's atmosphere "observation" and validation in this study

ERSSTv5	Extended Reconstructed SST version 5	SST observation product used to evaluate GMSSTr and NASSTr
GFDL	Geophysical Fluid Dynamics Laboratory	The institution of NOAA, who developed the CM2 model
GMOC	Global ocean meridional overturning circulation	The main theme in this study
MOC^n	The northern component of GMOC	The first Principal Component (PC1) of GMOC stream functions over the region north of 30°S
MOC^s	The southern component of GMOC	The PC1 of GMOC stream functions over the region south of 30°S
MOC^t	The tropical component of GMOC	The PC1 of GMOC stream functions over the region 30° S–30° N
GMSST	Global mean SST	An index of observed global mean SST
GMSSTr	Global mean SST residual	An index used to show the responses of observed SST on major volcanic eruptions
HadISST	Hadley Centre Sea Ice and Sea Surface Temperature Dataset	SST observation product used for CDA in this study
HF_{O2A}	Oceanic heat flux to the atmosphere	Feedback of the ocean to the atmosphere
IPCC	Intergovernmental Panel on Climate Change	An international organization created in response to the growing concern about human-induced climate change
IPMOC	Indo-Pacific meridional overturning circulation	The stream function of ocean meridional overturning circulation for the Indian Ocean and Pacific Ocean
LM2.1	Land Model version 2.1	A land component model of CM2
MOM4	Modular Ocean Model version 4	An ocean component model of CM2
MOVE	Meridional Overturning Variability Experiment	Volume transport data mooring observations at 16° N in the western Atlantic
NADW	North Atlantic Deep Water	The NADW index is defined as the average thickness between two isopycnals of $\sigma_{1.5}$ over the North Atlantic, see **Materials and Methods b3**.
NAO	North Atlantic Oscillation	A time series of the leading EOF of SLP anomalies over the Atlantic sector, 20°–80° N, 90° W–40° E
NAOC	The North Atlantic Changes	Volume transport data mooring observations at 47° N in the western Atlantic
NASSTr	North Atlantic SST residual	An index used to show the responses of observed SST over Northern Atlantic on major volcanic eruptions
NCAR	National Center for Atmospheric Research	The institution develops CESM model
NH	Northern Hemisphere	One half of the Earth in north of the equator
NOAA	National Oceanic and Atmospheric Administration	An agent of US federal government
OISST	Optimum Interpolation Sea Surface Temperature Dataset	SST observation product used for CDA in this study
ORAS5	Ocean Reanalysis System 5	Ocean reanalysis product as reference in this study
PC	Principal component, referred as PC1 (first), PC2 (second) etc.	The temporal evolution associated with each EOF
POP2	Parallel Ocean Program version 2	An ocean model component of CESM
Ps	Surface pressure	A basic variable of atmosphere state
RAPID	Rapid Climate Change: Meridional Overturning Circulation and Heatflux Array	A collaborative research project for measuring transport at 26.5°N in the Atlantic

RCP45	Representative Concentration Pathway 4.5	A medium-emission scenario, in which the radiative forcing level stabilizes at around 4.5 W/m² by 2100.
RMSE	Root mean square error	A measure of quantifying the differences between the estimated values and actual observed values
SAM	Southern Annular Mode	The principal mode of variability in the SH extra-tropics, describing ~30% of SH variability
SH	Southern Hemisphere	One half of the Earth in south of the equator
SLP	Sea level pressure	A basic variable of atmosphere state
SODA3	Simple Ocean Data Assimilation version 3.4.2	Ocean reanalysis product as reference in this study
SOI	Southern Oscillation Index	An index used to characterize the large scale SLP patterns in the tropical Pacific
SST	Sea Surface Temperature	A basic variable of ocean state
STD	Standard deviation	The dispersion of data relative to the mean
W_{A2O}	Atmospheric work exerted on the ocean	An important variable in atmosphere-ocean coupling process
WBCs	West boundary currents	An important ocean currents system
WOA	World Ocean Atlas	Ocean temperature and salinity observational climatology used for deep ocean restoring in CDA and validation of CDA results
ε_m	Kinetic energy dissipation rate	The diagnosed tropical diffusive mixing effects
$\sigma_{1.5}$	The potential density referenced to a depth of 1500 m	The isopycnals used to define NADW

Table S2. Description of reanalysis experiments.

Experiment	**Model information**	**Data constraint**	**Period**
CESM-HIS	**NCAR-CESM1.3** Atmospheric component: CAM5 1° × 1°, 26 layers Oceanic component: POP2 1° × 1°, 60 layers	1945–2006: historical radiative forcing 2007–present: RCP45 scenario	1945–present
CESM-CDA		Grided surface pressure (Ps) from ERA5, grided SST from HadISST and OISST, in-situ temperature and salinity profiles, restoring to World Ocean Atlas 2018 (WOA18) in deep ocean Radiative forcing is the same as CESM-HIS.	
CM2-HIS	**GFDL-CM2.1** Atmospheric component: AM2.1 2° × 2.5°, 24 layers Oceanic component: MOM4 1° × 1°, 50 layers	Same as CESM-HIS	
CM2-CDA		Same as CESM-CDA	

529 **Table S3.** Information of reanalysis products.

Reanalysis	Ocean model	Resolution	Forcing	Period
SODA3.4.2	Modular Ocean Model	0.5° × 0.5° 50 layers	ERA-interim	1980–2019
ECCOv4r3	Massachusetts Institute of Technology General Circulation Model	0.5° × 0.5° 50 layers		1992–2015
ORAS5	Nucleus for European Modelling of the Ocean	0.25° × 0.25° 75 layers		1958–present

530